

AD-A138 681

PROPAGATION EFFECTS IN SATELLITE-BASED SYNTHETIC
APERTURE RADARS(U) SRI INTERNATIONAL MENLO PARK CA
C L RIND ET AL. 01 MAR 83 DNA-TR-81-253

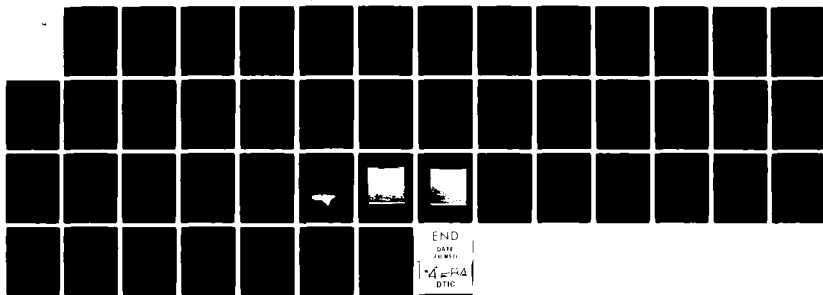
1/1

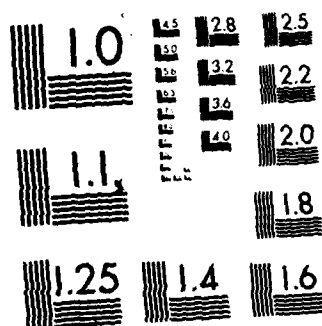
UNCLASSIFIED

DNA001-81-C-0010

F/G 17/9

NL





MICROCOPY RESOLUTION TEST CHART
NATIONAL BUREAU OF STANDARDS-1963-A

AD-E 301 336

12

AD A138681

DNA-TR-81-253

PROPAGATION EFFECTS IN SATELLITE-BASED SYNTHETIC APERTURE RADARS

C. L. Rino
V. H. Gonzalez
SRI International
333 Ravenswood Avenue
Menlo Park, California 94025

1 March 1983

Technical Report

CONTRACT No. DNA 001-81-C-0010

APPROVED FOR PUBLIC RELEASE;
DISTRIBUTION UNLIMITED.

MAR 8 1984

A

THIS WORK WAS SPONSORED BY THE DEFENSE NUCLEAR AGENCY
UNDER RDT&E RMSS CODE B322081466 S99QAXHA00002 H2590D.

Prepared for
Director
DEFENSE NUCLEAR AGENCY
Washington, DC 20305

DTIC FILE COPY

84 01 20 036

Destroy this report when it is no longer needed. Do not return to sender.

PLEASE NOTIFY THE DEFENSE NUCLEAR AGENCY,
ATTN: STTI, WASHINGTON, D.C. 20305, IF
YOUR ADDRESS IS INCORRECT, IF YOU WISH TO
BE DELETED FROM THE DISTRIBUTION LIST, OR
IF THE ADDRESSEE IS NO LONGER EMPLOYED BY
YOUR ORGANIZATION.



UNCLASSIFIED

SECURITY CLASSIFICATION OF THIS PAGE (When Data Entered)

REPORT DOCUMENTATION PAGE		READ INSTRUCTIONS BEFORE COMPLETING FORM
1. REPORT NUMBER DNA-TR-81-253	2. GOVT ACCESSION NO. AD-A138 6281	3. RECIPIENT'S CATALOG NUMBER
4. TITLE (and Subtitle) PROPAGATION EFFECTS IN SATELLITE-BASED SYNTHETIC APERTURE RADARS		5. TYPE OF REPORT & PERIOD COVERED Technical Report
		6. PERFORMING ORG. REPORT NUMBER SRI Project 2394
7. AUTHOR(s) C. L. Rino V. H. Gonzalez		8. CONTRACT OR GRANT NUMBER(s) DNA 001-81-C-0010
9. PERFORMING ORGANIZATION NAME AND ADDRESS SRI International 333 Ravenswood Avenue Menlo Park, California 94025		10. PROGRAM ELEMENT, PROJECT, TASK AREA & WORK UNIT NUMBERS Task S99QAXHA-00002
11. CONTROLLING OFFICE NAME AND ADDRESS Director Defense Nuclear Agency Washington, DC 20305		12. REPORT DATE 1 March 1983
		13. NUMBER OF PAGES 48
14. MONITORING AGENCY NAME & ADDRESS (if different from Controlling Office)		15. SECURITY CLASS (of this report) UNCLASSIFIED
		15a. DECLASSIFICATION DOWNGRADING SCHEDULE N/A since UNCLASSIFIED
16. DISTRIBUTION STATEMENT (of this Report) Approved for public release; distribution unlimited.		
17. DISTRIBUTION STATEMENT (of the abstract entered in block 20, if different from Report)		
18. SUPPLEMENTARY NOTES This work was sponsored by the Defense Nuclear Agency under RDT&E RMSS Code B322081466 S99QAXHA00002 H2590D.		
19. KEY WORDS (Continue on reverse side if necessary and identify by block number) Space-Based Radar Scintillation Nuclear Propagation		
20. ABSTRACT (Continue on reverse side if necessary and identify by block number) This report describes the effects of propagation disturbances on space-based synthetic aperture radars (SAR). Using a model developed earlier, we per- formed simulations to show the distortion of the radar ambiguity function for the SEASAT-A SAR. For moderate disturbance, an elevated sidelobe level causes a reduction in contrast. The SEASAT-A library of high-latitude data showed examples of this effect, one example of which is analyzed here in detail.		

DD FORM 1 JAN 73 1473

EDITION OF 1 NOV 65 IS OBSOLETE

UNCLASSIFIED

SECURITY CLASSIFICATION OF THIS PAGE (When Data Entered)

EXECUTIVE SUMMARY

Space-based, synthetic aperture radars (SAR) are being considered for a variety of strategic and tactical military missions. SARs in space can achieve resolutions comparable to practical optical instruments, and they are unaffected by clouds, weather, and darkness. The major obstacle to their use is the extensive data reduction required, although this problem is common to any advanced surveillance system and rapid progress in overcoming it is being made.

The azimuthal resolution of a SAR with a fixed antenna is limited by the beamwidth. Practical space-based systems can synthesize apertures approaching ~ 20 km. At L-band, the corresponding angular resolution is a few hundredths of milliradians; however, naturally occurring ionospheric disturbances can cause comparable amounts of angular jitter. Viewed another way, the spatial coherence scale of an L-band wave passing through a disturbed ionosphere can be reduced below 20 km.

To investigate the potential impact of the disturbances on SAR imagery, we have applied a general space-based radar model developed in the first phase of this contract. The resolution characteristics of a SAR are determined by the range-azimuth ambiguity function. By simulating ionospheric disturbances, we showed that moderate, naturally occurring disturbances degrade the azimuthal resolution primarily by raising the sidelobe level.

To look for evidence of the potential effects of such disturbances, we reviewed SAR data from the SEASAT-A satellite. One pass, which was coincident with incoherent-scatter radar operations that measured a highly structured F-region, showed an image region with a conspicuous contrast reduction. Other evidence of such effects during disturbed conditions also have been reported.

We believe these results to be the first demonstrated evidence of propagation-induced SAR image degradation. The results are consistent with predictions based on the SATCOM channel model that has been used extensively for analyzing communication and navigation systems. The inputs, however, draw heavily on our structure phenomenology program for the natural ionosphere.

More detailed simulations are planned to identify the characteristics of severe disturbances. This final report completes the development of the theoretical model.

TABLE OF CONTENTS

<u>Section</u>	<u>Page</u>
EXECUTIVE SUMMARY	1
LIST OF ILLUSTRATIONS	4
I INTRODUCTION	5
II A MODEL FOR EVALUATING PROPAGATION EFFECTS IN SPACE-BORNE SAR SYSTEMS	8
II' IONOSPHERIC EFFECTS	14
IV SEASAT-A DATA	24
V CONCLUSIONS AND RECOMMENDATIONS	36
REFERENCES	38



1A11

LIST OF ILLUSTRATIONS

<u>Figure</u>		<u>Page</u>
1	Functional Diagram of a Monostatic Radar System	5
2	Local Coordinate System for SAR Processing	9
3	Signal Spectrum for Range Compression	11
4	Schematic Representation of Scintillation Development . .	14
5	Scintillation Index and Coherence Measures for SEASAT-A SAR	18
6	Synthesized Antenna Beam for Propagation Disturbance with $C_s = 10^{22}$	20
7	Synthesized Antenna Beam for Propagation Disturbance with $C_s = 10^{23}$	21
8	Synthesized Antenna Beam for Propagation Disturbance with $C_s = 10^{24}$	22
9	SAR Image Swath for SEASAT-A Revolutions 1279 and 1236	28
10	Topographical Map of Region Encompassing SAR Image . . .	29
11	Digitally Processed Image for Revolution 2379	30
12	Digitally Processed Image for Revolution 1236	31
13	Map Grid Showing Locations of Degraded SAR Image and Chatanika Meridian	32
14	Chatanika Radar Map of Meridional Ionization Distribution Prior to SAR Image	34
15	Chatanika Radar Map of Meridional Ionization Distribution After SAR Image	35

I INTRODUCTION

Space-based radar (SBR) systems have been proposed for future CONUS defense, surveillance, and tactical battle-support functions. These systems, however, may have to operate in naturally or nuclear-disturbed propagation environments. This final report describes the effects of propagation disturbances on space-based synthetic aperture radars (SARs), which are becoming increasingly more important for strategic and tactical support missions.

In Topical Report 1,^{1*} we developed a general mathematical formalism for using the satellite communications model to simulate SBR propagation effects and/or to calculate measures of average performance degradation. The functional elements of a monostatic radar system are diagrammed in Figure 1, which is taken from Topical Report 1.

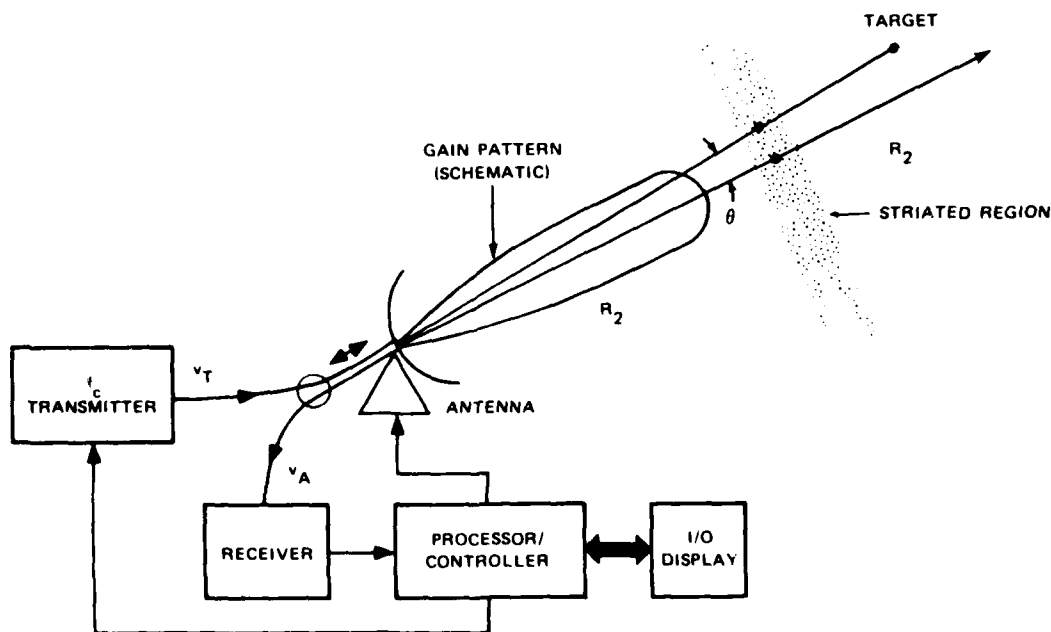


FIGURE 1 FUNCTIONAL DIAGRAM OF A MONOSTATIC RADAR SYSTEM

*References are listed at the end of the report.

The SATCOM model characterizes the propagation effects on a single path in terms of a time-varying impulse response or the equivalent transfer function. To accommodate a two-way path fully, the SATCOM channel model effectively must be evaluated twice, although the differences between the paths can be accommodated by scaling the independent variable appropriately.

The computation of average performance measures for a two-way path can be very complicated. However, in Topical Report 1 we showed that, under the severely disturbed conditions of primary concern, the forward and return paths are uncorrelated. Thus, average performance measures generally can be constructed from products of average measures on the individual paths.

In addition to the two-way path problem, propagation effects in SBR systems are more critically dependent on angular deviation than are propagation effects for SATCOM, where the source (target) location generally is known. This is particularly true for SARs.

The model developed in Topical Report 1 uses a discrete array of noninteracting point sources to simulate an arbitrary antenna configuration. For a dense distribution of radiators (or receivers), the more familiar aperture distribution functions can be recovered by replacing summations with integrals.

The actual propagation effects are accommodated by applying the appropriate channel transfer function to the radar signal. For a narrow-band signal, the propagation effects are multiplicative. At any instant in time, the effect is to convolve the gain pattern of the antenna with a random function. The average distortion of the gain pattern is obtained by computing the Fourier transform of the aperture distribution multiplied by the mutual coherence functions [see Eq. (33) in Topical Report 1]. The principal parameter is the size of the aperture compared with the spatial coherence scale.

The temporal variations of the signal mainly affect the sensitivity of the system as distinct from its resolving power. In effect, the target cross section fades--a problem that has been treated extensively in radar

theory.^{2,3} Similarly, loss of phase coherence limits the effective coherent integration time.⁴ Finally, loss of frequency coherence limits the achievable range resolutions. Such effects are not fundamentally different from their counterparts in SATCOM systems, and detailed simulations are ultimately required for performance evaluations.

In the remainder of this report, we consider the performance degradation of satellite-borne SAR systems. The SAR method achieves high resolutions (comparable to practical optical instruments in space) by coherently processing the radar returns over periods approaching the time a target-element remains within the beam. Coherent processing is used to compensate for the phase drift induced by the satellite motion. Propagation disturbances cause both phase and amplitude errors that distort the synthesized beam.

We have divided our treatment of the problem into three parts. In Section II, we develop a model that includes all the essential elements of a SAR system; we used the SEASAT-A SAR as a model. The satellite was operational only for a little more than three months commencing in July 1978, but it produced a large data base for demonstrating propagation effects. In Section III, we used the SATCOM model with typical ionospheric parameters to determine the likelihood of significant SAR performance degradation due to natural disturbances.

Our analysis shows that only the most intense high-latitude disturbances are likely to produce a detectable SAR image degradation. More severe disturbances would be expected near the geomagnetic equator. In collaboration with staff members from Research Development Associates (RDA) who were working with SEASAT data for other reasons, we performed a search of the SEASAT-B library of optically processed data. One pass that showed a conspicuous image degradation coincided, fortuitously, with a set of incoherent-scatter radar measurements. The radar data showed a prominent F-layer enhancement with the characteristics that have been consistently associated with enhanced scintillation.

In Section V we discuss the effects of more severe propagation disturbances and future effort to identify and mitigate the effects of propagation disturbances.

II A MODEL FOR EVALUATING PROPAGATION EFFECTS IN SPACE-BASED SAR SYSTEMS

The principal of SAR processing is simple. A linear array of discrete elements can be focused by adjusting the phase of the individual elements so that the returns from a signal emanating from the focal point have the same phase. Alternatively, the complex signal from a single element can be recorded as it moves along the axis of the linear array, and the appropriate phase adjustments can be made ex post facto. The beamwidth of a fixed antenna element imposes a limitation on the maximum aperture that can be synthesized.

For example, let the aperture width of the antenna element be L_E . The maximum element separation that can contribute to a focus at R is

$$L_{\max} \approx \frac{R\lambda}{L_E} \quad (1)$$

The spatial resolution of the synthesized array is

$$\Delta y' \approx \frac{R\lambda}{2L_{\max}} = \frac{L_E}{2} \quad (2)$$

Because the SAR antenna is used for both transmission and reception, the effective aperture is halved; hence, the factor of 2 in Eq. (2).

For the SEASAT-A satellite, a phased array with an effective aperture of ~ 12 m was used; thus, the intrinsic resolution is ~ 6 m. The aperture is traversed in 2 s. In practice, four 4-km segments are processed separately and then averaged to reduce cross section variations caused by the changing aspect angle. Thus, ~ 25 m is the azimuth resolution usually achieved for digitally processed SAR images.

High resolution in the cross-track direction is achieved by using pulse compression. The transmitted signal has the form

$$P(t) = \operatorname{Re} \left\{ \operatorname{rect} \left(\frac{t}{T} \right) \exp[2\pi i (f_0 t + K_r t^2)] \right\} \quad (3)$$

For SEASAT-A,

$$\begin{aligned} T &= 33.9 \text{ s} \\ K_r &= 0.562 \text{ MHz/s} \\ f_o &= 11.25 \text{ MHz} \end{aligned}$$

Details of the SEASAT-A signal structure and data processing can be found in References 5 and 6. The corresponding complex signal will be denoted by $p(t)$.

To model the return signal, we consider the coordinate system shown in Figure 2, where $r(t)$ is the distance from the satellite at time t to

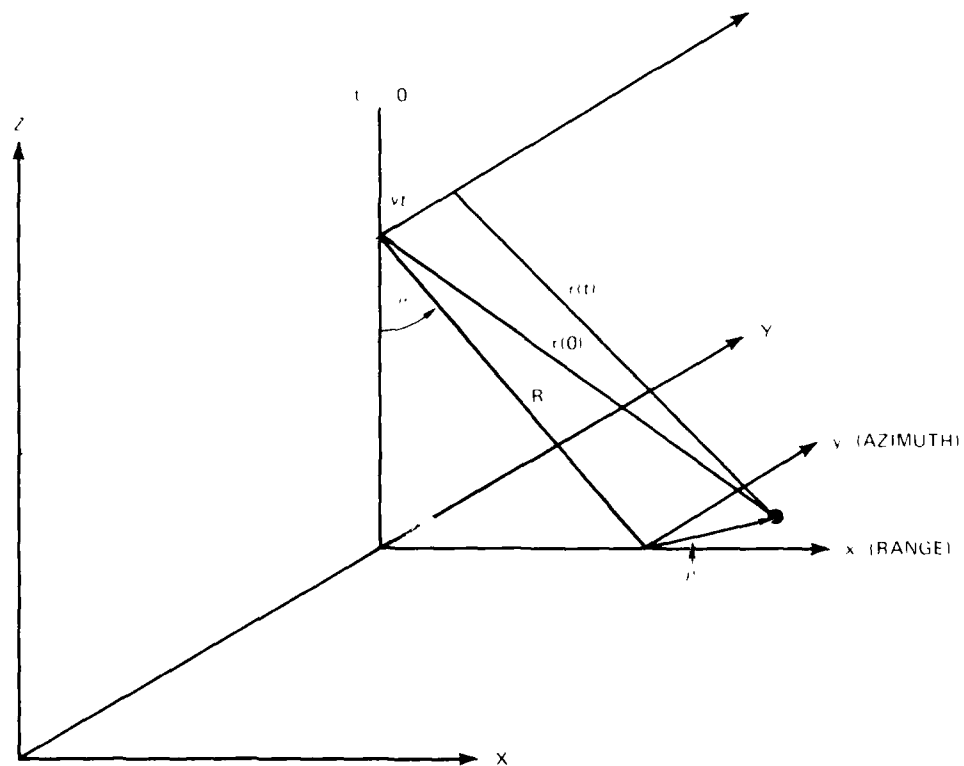


FIGURE 2 LOCAL COORDINATE SYSTEM FOR SAR PROCESSING

a fixed point (x, y) on the ground. Thus,

$$r(t) = \left[(R \sin \theta + x)^2 + (y - vt)^2 + (R \cos \theta)^2 \right]^{\frac{1}{2}} \\ \approx R + x \sin \theta - \frac{yvt}{R} + \frac{\rho^2 + (vt)^2}{2R} \quad (4)$$

where $\rho = (x^2 + y^2)^{\frac{1}{2}}$. The return signal from a single point target at ρ admits the representation

$$S(t) = \text{Re}\{p(\tau) * g(t, \tau) \sigma(\vec{\rho}) \exp[4\pi i r(t)/\lambda]\} \quad (5)$$

where $\sigma(\vec{\rho})$ is the complex scattering coefficient assumed to be frequency independent over the frequency band of the pulse. Ionospheric effects are accommodated by convolving $p(\tau)$ with the time-varying impulse function $g(t, \tau)$. Alternatively, we can write

$$p(\tau) * g(t, \tau) = \int \hat{p}(f) h(t, f_c + f) \exp(2\pi i f \tau) df \quad (6)$$

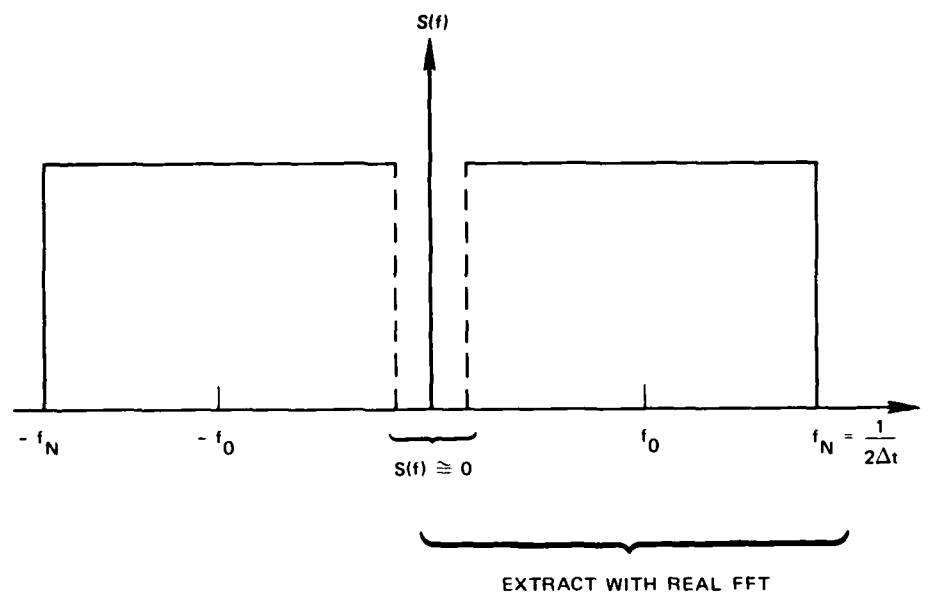
where $h(t, f)$ is the time-varying transfer function and

$$g(t, \tau) = \int h(t, f_c + f) \exp(2\pi i f \tau) df \quad (7)$$

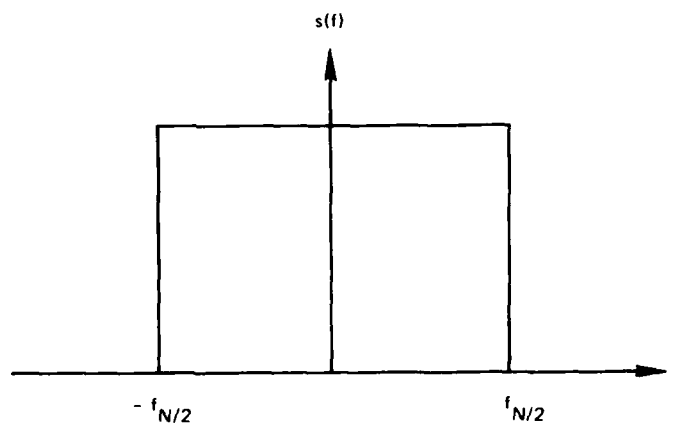
In the SEASAT-A data reduction, bursts of 13,680 samples over a 300.46- μ s interval are recorded every interpulse period of $T_p \approx 600 \mu$ s; thus, $1/\Delta t = 45$ MHz. The spectral extent of the sampled signal is shown in Figure 3(a). The data are processed by first performing a 4096-point real Fast Fourier Transform, which generates 2048 complex frequency samples spanning $f = 0$ to $f_N = 22.5$ MHz. To generate the complex signal, a cyclic shift of the Fourier components is performed as illustrated in Figure 3(b).

The complex signal is then multiplied by $p^*(n\Delta f)$. If the time-bandwidth product is large, the inverse Fourier transform of $|p|^2$ is well approximated by

$$p_c(t) = \frac{K_r T_r^2 \sin(\pi K_r T t)}{\pi K_r T t} \quad (8)$$



(a) SPECTRUM OF SAMPLED SIGNAL



(b) SPECTRUM OF COMPLEX SIGNAL

FIGURE 3 SIGNAL SPECTRUM FOR RANGE COMPRESSION

In practice, the radial component of the satellite motion causes a Doppler shift that manifests itself as an uncertainty in f_0 , and a time-consuming iterative procedure must be used. For our purposes here, however, this subtlety can be ignored.

We note, however, that over the 300- μ s data interval, changes in $r(t)$ are negligible, as are changes in $g(t, \tau)$ with t . Thus, the pulse compression operation affects only $p(t)$ in Eq. (5); moreover, $\Delta t = (K_T)^{-1}$. In range delay units, we can write

$$s_c(j, \ell) = \iint p_c(j\Delta R - x\sin\theta - \eta_\ell) * g(\ell T_p, j\Delta R - x\sin\theta - \eta_\ell) \times \exp(4\pi i \frac{\eta_\ell}{\lambda}) \sigma(\vec{\rho}) d\vec{\rho}, \quad (9)$$

where T_p is the interpulse period; then,

$$\eta_\ell = -y \frac{v T_p \ell}{R} + \frac{1}{2} \frac{\rho^2 + (v T_p \ell)^2}{R}, \quad (10)$$

and we have integrated over all scatterers.

The fact that η_ℓ appears in the argument of $p_c(x)$ greatly complicates the azimuth compression operation. The range cell for which the azimuth compensation η_ℓ is to be applied changes with ℓ . To make this explicit, we define

$$j(\ell) = [(x\sin\theta - \eta_\ell)/\Delta R]_I, \quad (11)$$

where $[\cdot]_I$ denotes the nearest integer value. The processed signal for a target area centered at (x', y') is

$$\hat{\sigma}(\vec{\rho}') = \frac{1}{N_p} \sum_{\ell=0}^{N_p-1} s_c[j'(\ell), \ell] \exp(-4\pi i \eta'_\ell / \lambda). \quad (12)$$

Because of the phase fluctuations of the target area, the quantity of interest is $\overline{|\hat{\sigma}(\vec{\rho}')|^2}$, where the overbar denotes an average.

One usually assumes that the target-scattering function is a random process that is uncorrelated from one resolution cell to the next. We define the ambiguity function as

$$A(\vec{\rho}, \vec{\rho}') = \frac{1}{N_p} \sum_{\ell=0}^{N_p-1} p_c * g(\ell T_p, j'(\ell) \Delta R - x \sin \theta - \eta_\ell) \times \exp[4\pi i(\eta_\ell - \eta'_\ell)/\lambda] \quad (13)$$

Using the assumption of uncorrelated resolution cells, it follows that

$$\langle |\hat{\sigma}(\vec{\rho}')|^2 \rangle = \iint \langle |A(\vec{\rho}, \vec{\rho}')|^2 \rangle \langle |\sigma(\vec{\rho})|^2 \rangle d\vec{\rho} \quad (14)$$

The ionospheric disturbance potentially affects both the range, x , and azimuth, y , coordinates; however, for naturally occurring ionospheric disturbances, the range distortion is negligible, as we shall show in the next section. It should also be noted that insofar as evaluating the effects of propagation disturbances are concerned, there is no loss of generality in assuming that the compressed pulse, p_c , was actually transmitted.

III IONOSPHERIC EFFECTS

The mathematics of wave propagation in randomly irregular media have been treated extensively in published papers,^{7,8} as have its applications to systems effects.⁹ Here we shall only review these results to justify our choice parameters used in evaluating the effects of naturally occurring ionospheric disturbances. Scintillation is essentially an interference phenomenon as is illustrated schematically in Figure 4.

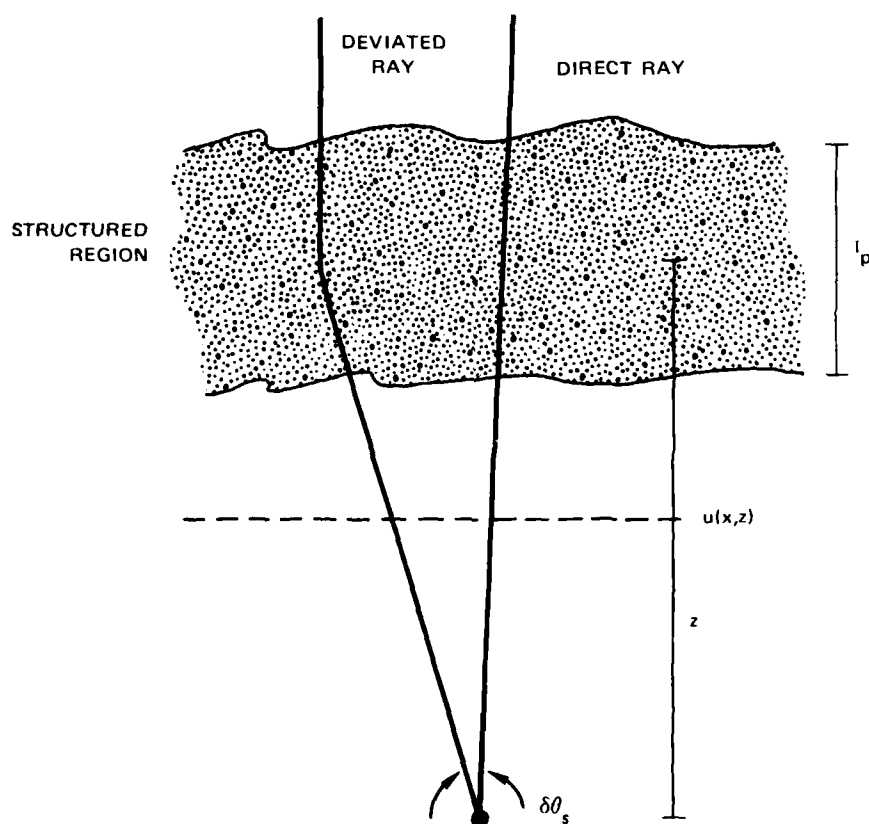


FIGURE 4 SCHEMATIC REPRESENTATION OF SCINTILLATION DEVELOPMENT

The spatial wavenumber spectrum of the complex field $u(\vec{p}, z)$ characterizes the angular distribution of the scattered waves. Formally, the wavenumber spectrum is the Fourier transform of the mutual coherence

function which has the particularly simple mathematical form

$$\langle u(\vec{\rho}, z) u^*(\vec{\rho}', z) \rangle = \exp\{-\frac{1}{2} D(\Delta\vec{\rho})\} \quad , \quad (15)$$

where $D(\Delta\vec{\rho})$ is the phase structure function. The in-situ irregularities are characterized by a three-dimensional power spectral density function of the form

$$\Phi(q) = C_s q^{-(p+1)} \quad , \quad (16)$$

where

$$C_s = 8\pi^{3/2} q_o^{p-2} \frac{\Gamma\left(\frac{p+1}{2}\right)}{\Gamma\left(\frac{p-2}{2}\right)} \langle \Delta N_e^2 \rangle \quad (17)$$

relates the turbulence parameter C_s to the electron density variance via an outer scale wavenumber q_o . The corresponding phase variance for a path of length ℓ_p is

$$\langle \delta\phi^2 \rangle = 2\sqrt{\pi} r_e^2 \lambda^2 \frac{\Gamma\left(\frac{p-1}{2}\right)}{\Gamma\left(\frac{p-2}{2}\right)} q_o^{-1} [\ell_p G \langle \Delta N_e^2 \rangle] \quad , \quad (18)$$

where r_e is the classical electron radius and G is a geometric factor that accounts for irregularity anisotropy. The square brackets denote an average value over the propagation path.

In terms of these model parameters, it can be shown that

$$D(y) = r_e^2 \lambda^2 \ell_p C_s C(p) |y|^{\max(2, p-1)} \quad 2 \leq p \leq 4 \quad , \quad (19)$$

where

$$C(p) = \frac{1}{2\pi} [0.25 p^2 - 2.25 p + 5.5] \quad . \quad (20)$$

We define ℓ_o so that

$$D(\ell_o) = 2 \quad . \quad (21)$$

The corresponding temporal coherence time is given as

$$t_o = \frac{\ell_o}{v_{eff}} \quad (22)$$

If we let $p = 3$, Eq. (22) is equivalent to Eq. (2) in Wittwer.⁹ In that case, $\ell_o \propto f$.

The frequency coherence can be estimated by noting that the average angular deviation is proportional to $(\ell_o k)^{-1}$, which we can equate with $\delta\theta_s$ in Figure 4. The path difference for small $\delta\theta_s$ is $\frac{z\delta\theta_s^2}{2}$. The corresponding delay spread is given as

$$\Delta\tau = \frac{z\delta\theta_s^2}{2c} = \frac{z}{ck^2\ell_o^2} \quad (23)$$

The corresponding frequency spread f_o is defined as

$$f_o = \frac{1}{\Delta\tau} = \frac{ck^2\ell_o^2}{z} \quad (24)$$

Again, if we let $p = 3$, Eq. (24) is equivalent to Eq. (3) in Wittwer⁹ for which $f_o \propto f^3$. In any case, the coherence bandwidth changes much more rapidly with frequency than does the spatial coherence, ℓ_o .

The general form of frequency correlation function does not admit simple mathematical representation. Wittwer⁹ has derived a representation valid for $p \approx 3$. An integral representation based on the phase screen model was used to interpret data from the Wideband satellite.¹⁰ The main differences between these models lie in the approximations that have been used and the parameter ranges that have been emphasized.

The SATCOM model for nuclear effects assumes a q^{-3} power law to an outer scale wavenumber corresponding to ~ 10 km. For the ionosphere, a two-component power law seems most representative.^{11,12} For intermediate-scale structures between 10 km and 500 m, a shallowly sloped power law with $2 < p < 3$ applies. For sizes smaller than 500 m, a much steeper slope, $3 < p < 5$, applies.

A detailed analysis of the scintillation effects of a two-component power law has been performed.¹³ The resultant scintillation structure depends critically on the Fresnel radius r_f . If r_f is smaller than the scale of the break frequency, the scintillation structure is essentially the same as a single component power law with a steep slope ($p > 3$); r_f is greater than the scale of the break frequency but less than the outer scale, the break acts much like an outer scale cutoff. Finally, as the Fresnel radius increases toward the outer scale, the low-frequency portion of the spectrum, where most of the spectral intensity lies, dominates the signal moments; however, the high-frequency components of the scintillation intensity spectrum follows the steeply sloped portion of the integrated phase spectrum.

At L-band and higher frequencies, typical Fresnel radii are smaller than the scale of the break frequency q_b . Thus, the scintillation structure has the characteristics of a steeply sloped power law environment. To extend Eq. (16) beyond q_b , we can use

$$\Phi(q) = \begin{cases} C_s q^{-p_\ell} & q_o < q \leq q_b \\ C_s q_b^{(p_h - p_\ell)} q^{-p_h} & q > q_b \end{cases} \quad (25)$$

It follows that

$$C'_s = C_s q_b^{(p_h - p_\ell)} \quad (26)$$

is the effective turbulent strength for the transition scale structure.

In Figure 5 we have plotted ℓ_o and f_o with the S_4 scintillation index using both the intermediate-scale (p_e) and the transitional scale (p_h) power law components. A break frequency of 500 m was used, which exceeds the median value of 750 m reported by Basu et al.¹² Thus, the curves in Figure 5 should bracket the actual coherence scales. In general, the effect of the steeply sloped transition scale is to increase both the coherence bandwidth and the spatial coherence. In all cases, however, the coherence bandwidth remains well beyond the frequency band

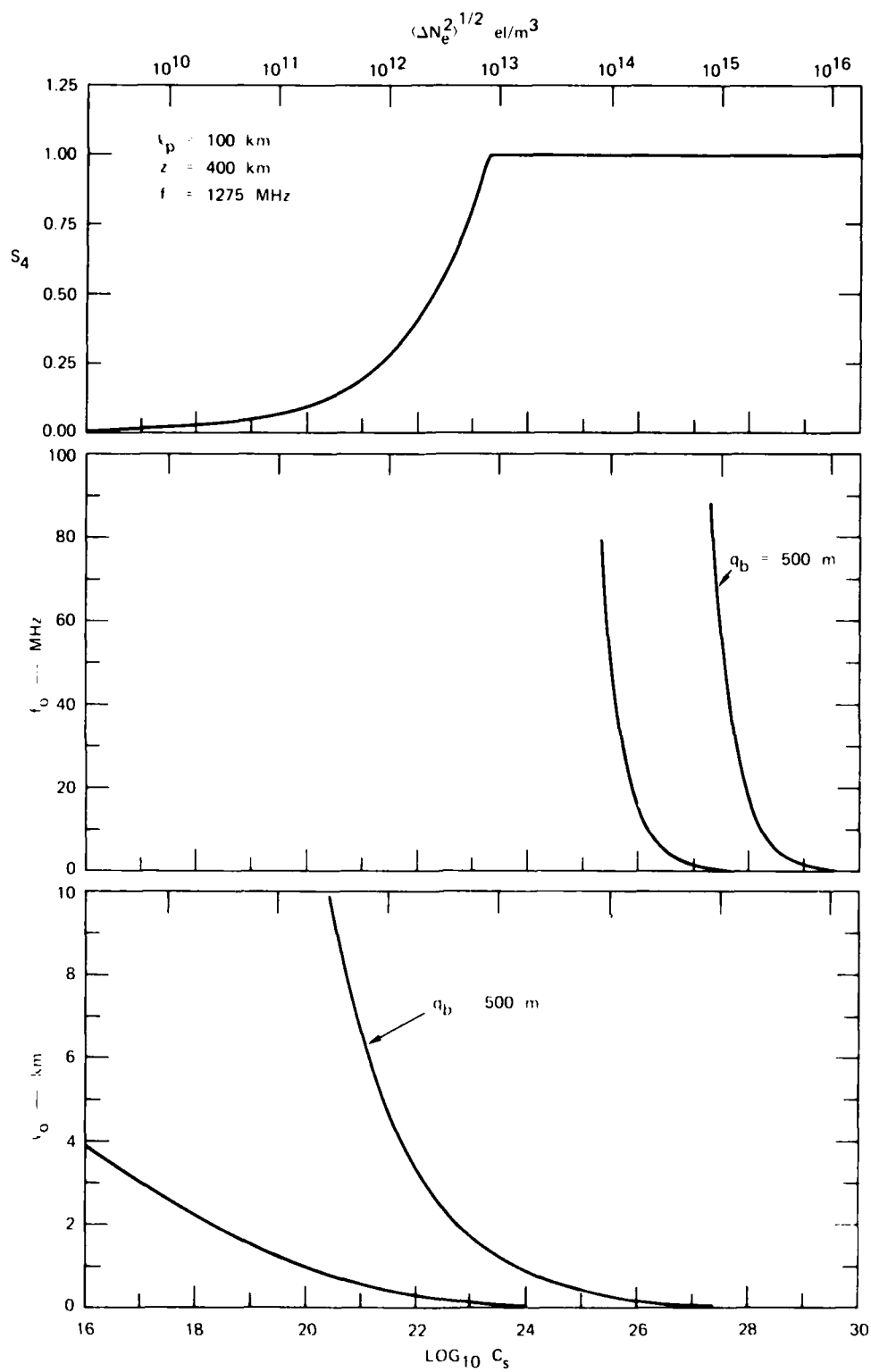


FIGURE 5 SCINTILLATION INDEX AND COHERENCE MEASURES FOR SEASAT-A SAR

of the chirp pulse. Under such conditions, the ionosphere causes only a pulse-to-pulse variation, and $p_c * g$ in Eq. (13) can be replaced by the simple product $p_c(\tau)h(\ell T_p, f_c)$, which follows from Eq. (7).

The spatial coherence, however, can be reduced below the limits of space-based SAR apertures. To evaluate the effect of propagation disturbances in such cases, we have simulated the ambiguity function as defined by Eq. (13), using the parameters listed in Table 1. For simplicity, we have ignored the range migration effect so that the propagation-induced distortion is confined entirely to the azimuth coordinate. Single-phase screen simulations based on the two-component power law were used to generate realizations of $h(\ell T_R, f_c)$.

Table 1
SEASAT-A PARAMETERS

Symbol	Name	Value
f	Frequency	1275 MHz
T_p	Interpulse period	$(1464)^{-1} s$
v	Velocity	8.78 km/s
N_p	Number of pulses	2667
L	Synthesized aperture size	16 km
R	Slant range	830 km
θ	Beam offset	20°
Δx	Range step	~ 8 m (not used in simulation)
Δy	Azimuth step	$vT_p = 6$ m

Representative results for progressively increasing C_s values are shown in Figures 6 through 8. The effect of the propagation disturbances is to lower the peak of the main lobe and raise the sidelobe level. Broadening of the main lobe, which one would associate with loss of resolution, is not significant. Thus the propagation effects act to reduce contrast rather than to defocus the SAR image. This is an important distinction for processing algorithms and mitigation techniques.

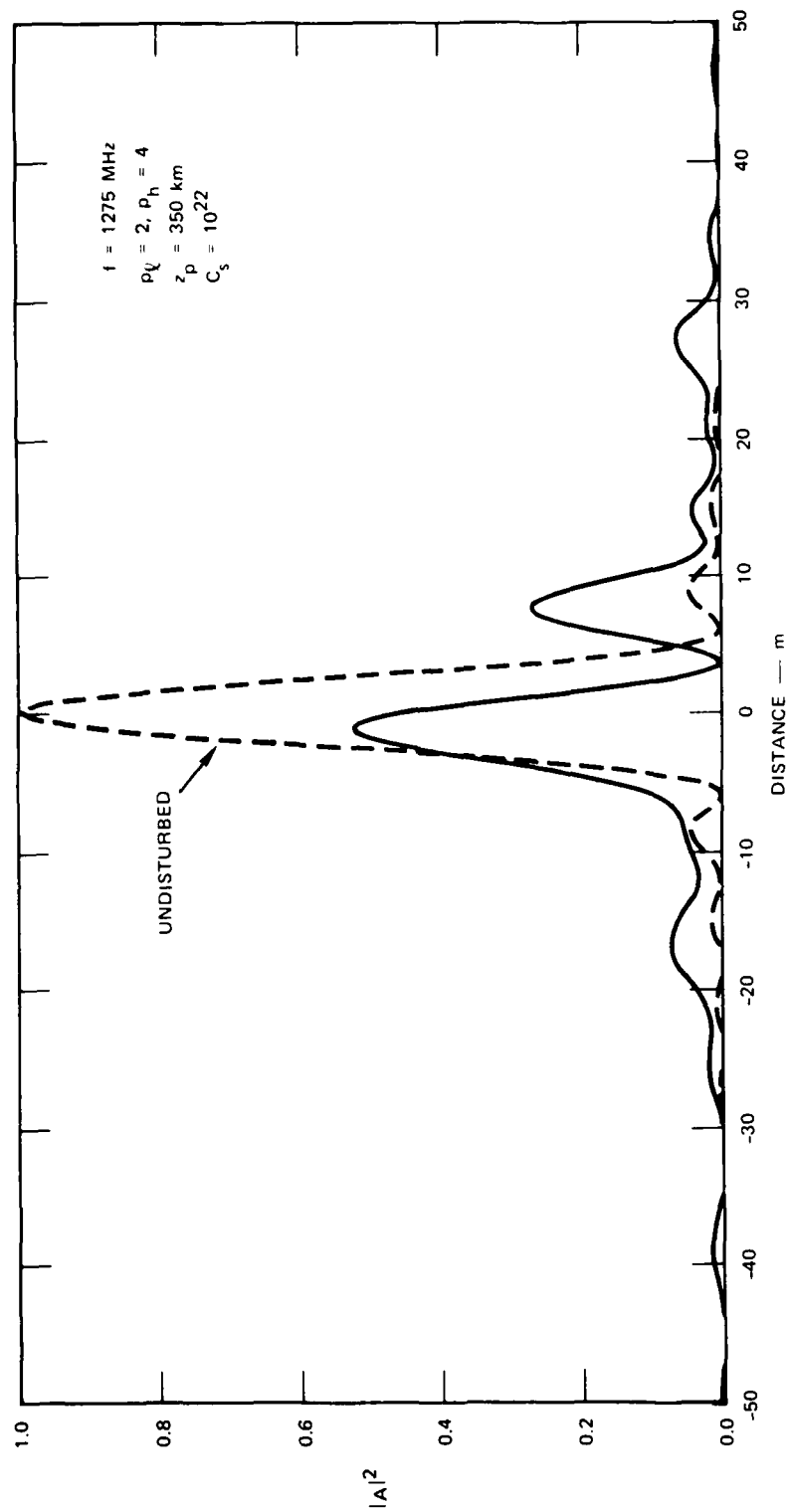


FIGURE 6 SYNTHESIZED ANTENNA BEAM FOR PROPAGATION DISTURBANCE WITH $C_s = 10^{22}$

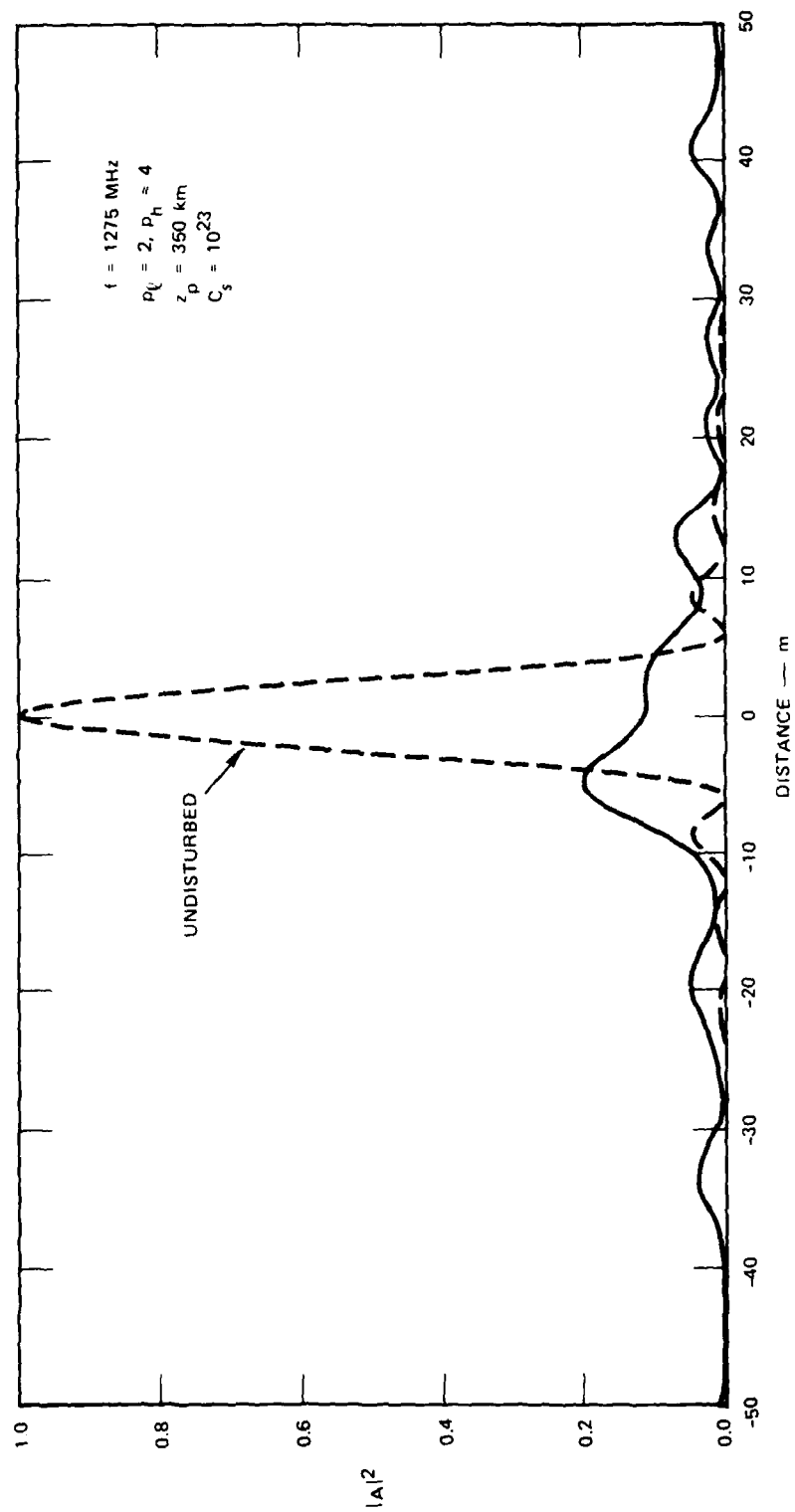


FIGURE 7 SYNTHESIZED ANTENNA BEAM FOR PROPAGATION DISTURBANCE WITH $C_s = 10^{23}$

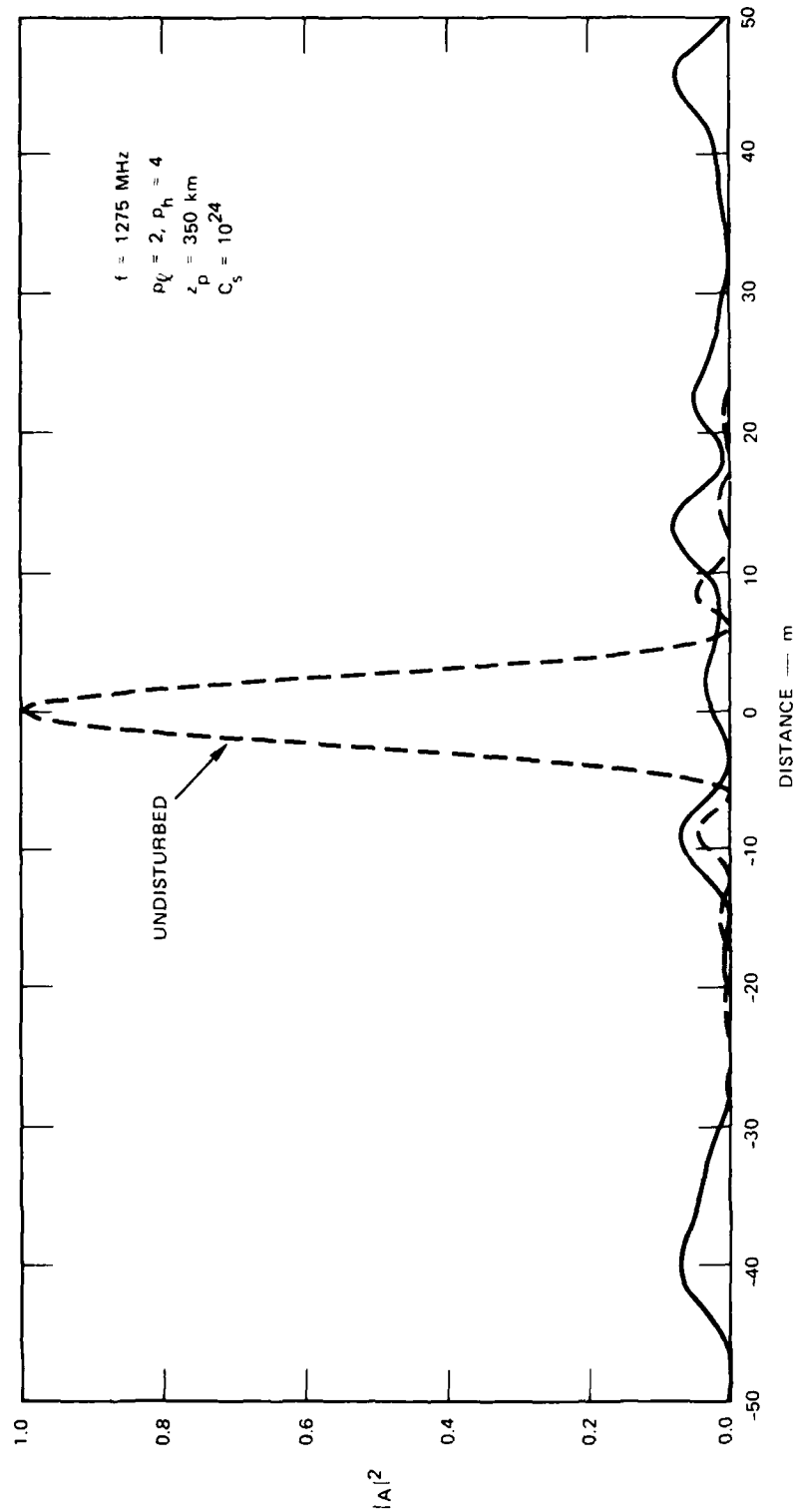


FIGURE 8 SYNTHESIZED ANTENNA BEAM FOR PROPAGATION DISTURBANCE WITH $C_s = 10^{24}$

Other analyses of propagation disturbances in SARs have been made,¹⁴ these analyses confined the errors entirely to the phase of the signal. A least-squares estimate of the linear and quadratic phase terms was obtained, together with rms value of the residual called the integrated sidelobe ratio. Consistent with our own results, the integrated sidelobe ratio was found to be the most serious concern for SAR image degradation.

IV SEASAT-A DATA

A large number of high-latitude SAR images were recorded by the SEASAT-A satellite when it was operational in 1978. A systematic search of the SEASAT library of passes was performed to identify pass segments where propagation disturbances were likely. In the initial sorting, we accepted all pass segments that fell within the auroral zone or polar cap within four hours of local midnight. The auroral-zone passes were then further divided into nighttime Alaska sector and nighttime non-Alaska sector passes.

The SEASAT passes that satisfy these criteria are summarized in Table 2. These passes collected data during the most likely periods for auroral activity. We made no attempt to further sort the data on the basis of magnetic activity or other indicators of auroral activity; rather, we decided to make a systematic visual survey of the optically processed SEASAT images to identify any degradation that could be attributed to auroral propagation disturbances.

Because several factors that are difficult to control affect the quality of the optical images, we sought distinct changes within a single image that could not be immediately associated with actual changes in the terrain and other factors. We paid careful attention to operator logs and comments by personnel familiar with the detailed processing techniques.

Dr. Victor Gonzalez of SRI and Dr. Dean Liskow of RAD paid two visits to the Jet Propulsion Laboratory (JPL). About 60 of the optically processed SEASAT passes from the candidate subset were examined. The optically reduced data are presented in the form of four strips of (negative and positive prints) film, each several feet long. The quality of the data is good most of the time, and the images are clear.

The resolution in the data studied was of the order of 10 to 20 km per inch. Thus, the resolution did not allow examination of small details of less than about 100 m. Rivers, mountain ranges, and coast lines provided good edges for comparison during different passes because

Table 2

CONDIDATE PASSES FOR AURORAL PROPAGATION DISTURBANCES

(a) Alaska Auroral Zone (primary candidate)			(b) Polar Cap (supplementary passes)			(c) Non-Alaska Auroral Zone (Last Resort)		
ID #	Start (UT)	Stop (UT)	ID #	Start (UT)	Stop (UT)	ID #	Start (UT)	Stop (UT)
001	1218	1224	086	INCLUDE FULL PASS	INCLUDE FULL PASS	016	1130	1136
002	1225	1231	092			025	1000	1006
004	1332	1338	097			032	1037	1043
013	1200	1206	104			038	1432	1438
028	1246	1252	119			044	1014	1021
037	1253	1259	124			045	1152	1157
040	1401	1407	128			048	0944	0951
046	1331	1337	132			089	2125	2131
052	1411	1415	137			107	2132	2137
099	1329	1333	142			121	2139	2145
106	1437	1443	145			129	1343	1349
146	1457	1503	149			143	1351	1356
151	1428	1434	161			153	2231	2237
163	1435	1441	169			165	2237	2243
174	1439	1445	173			176	2134	2140
188	1654	1700	181			218	2340	2342
202	1520	1524	195			233	2353	2354
303	1026	1031*	199			248	0005	0007
330	1039	1043*	276			264	0017	0020
355	1052	1055	280			274	0030	0033
419	1336	1346	283			308	2355	2357
427	1129	1134	285			319	0108	0111
442	1349	1359	288			344	0008	0011
445	1705	1713	296			344	0121	0124
450	1142	1147	304			352	0230	0232
465	1402	1411	315			361	0021	0023
468	1717	1726	322			375	1626	1632
474	1155	1202	340			377	0103	0107
			349			398	1639	1645
			357			400	0116	0120
			366			422	1652	1701
			374			439	0031	0037
			381			462	0044	0045
			389			480	0124	0130
			397					
			404					
			412					
			428					
			436					
			451					
			459					
			476					

* Meridian

the data were frequently taken over the same area. In some instances, however, the configuration of the ice in rivers changed enough to make the recognition of details difficult.

Examination of the pictures showed that they contained times (or areas) in which the data were deficient to various degrees, and sometimes were missing completely. Discussion with JPL staff familiar with the acquisition of data disclosed that several reasons could account for data degradation. For example, dynamic behavior of the satellite could be one reason. When the data are transmitted to the ground-monitoring stations, the ground receivers have antennas with different gains and receivers with different characteristics that add "noise" to the analog data received. The details of the optical processor also have adjustments (such as focusing) that also may occasionally add noise to the data.

Nonetheless, we isolated a pass that did contain the expected characteristics of a propagation disturbance:

ID No.	330
Revolution No.	1236
Date	21 Sept 1979
UT	1041:50 to 1042:10.

We also located an unperturbed pass that covered the same area:

ID No.	355
Revolution No.	1279
Date	24 Sept 1979
UT	1054:33 to 1054:33.

The characteristics of the degradation are as follows:

- The degraded area is localized.
- The degraded area does not include all ranges.
- The boundaries of the degraded area are not perpendicular to the direction of satellite motion.

Figure 9 shows the image swath of the two SEASAT-A passes superimposed on a map of Alaska and northern Canada; the shaded area is the region of interest. Figure 10 shows a topographical map of the image area, which lies northeast of Fort Yukon, Alaska.

Figure 11 shows the digitally processed normal SAR image. The Porcupine and the Coleen Rivers, as well as the nearby lakes, correlate very well with the topographical map. The striking map-like character of SAR radar images is well known. Figure 12 is a radar image of the same area but recorded several days earlier. This image shows a broad wedge-shaped region where there is a distinct loss of contrast but no perceptible loss of resolution. This type of degradation is consistent with the analysis presented above in Section III.

Through an extremely fortuitous set of circumstances, the Chatanika radar, which is located near Fairbanks, Alaska, was operating during the period the SAR image shown in Figure 12 was recorded. The radar was performing a routine 24-hour run in a mode that included elevation scans as well as multiposition measurements for drifts. From the elevation scan data, it is possible to map the distribution of ionization in the magnetic meridian. Such elevation scans have been used extensively to study unstable F-region "blobs"; indeed, they provided the first demonstration of the association of F-region structure and scintillation.¹⁵

Figure 13 shows the track of the subsatellite point and a track displaced 20° from the orbit plane as viewed from the satellite. The points on the subsatellite track are 20 s apart. The numbers on the 20° track are the geometrical scintillation enhancement factors for 10:10:1 sheets.¹⁶ It is interesting to note that this pass is not favorably oriented for a strong geometrical enhancement in the image region.

The dark bar locates the meridian plane of the radar scan. The area of the SAR image is outlined, and the region of the degradation is shaded. The plane of the meridian scan intercepts the image region; however, the F-region penetration point of the structure region lies to the east of the ground image area. It is significant that the degradation was observed as an east-west protrusion into the image region.

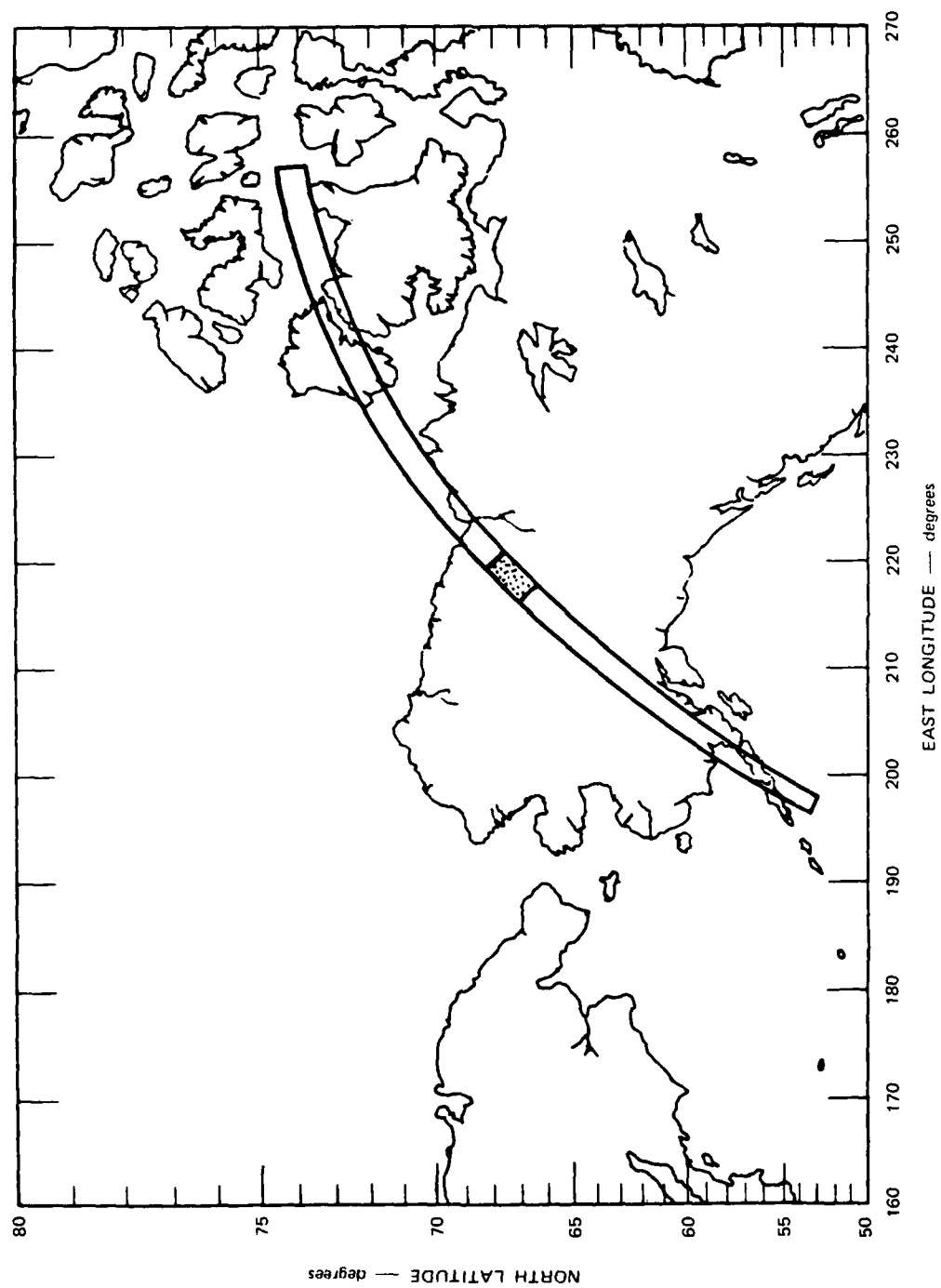


FIGURE 9 SAR IMAGE SWATH FOR SEASAT-A REVOLUTIONS 1279 AND 1236

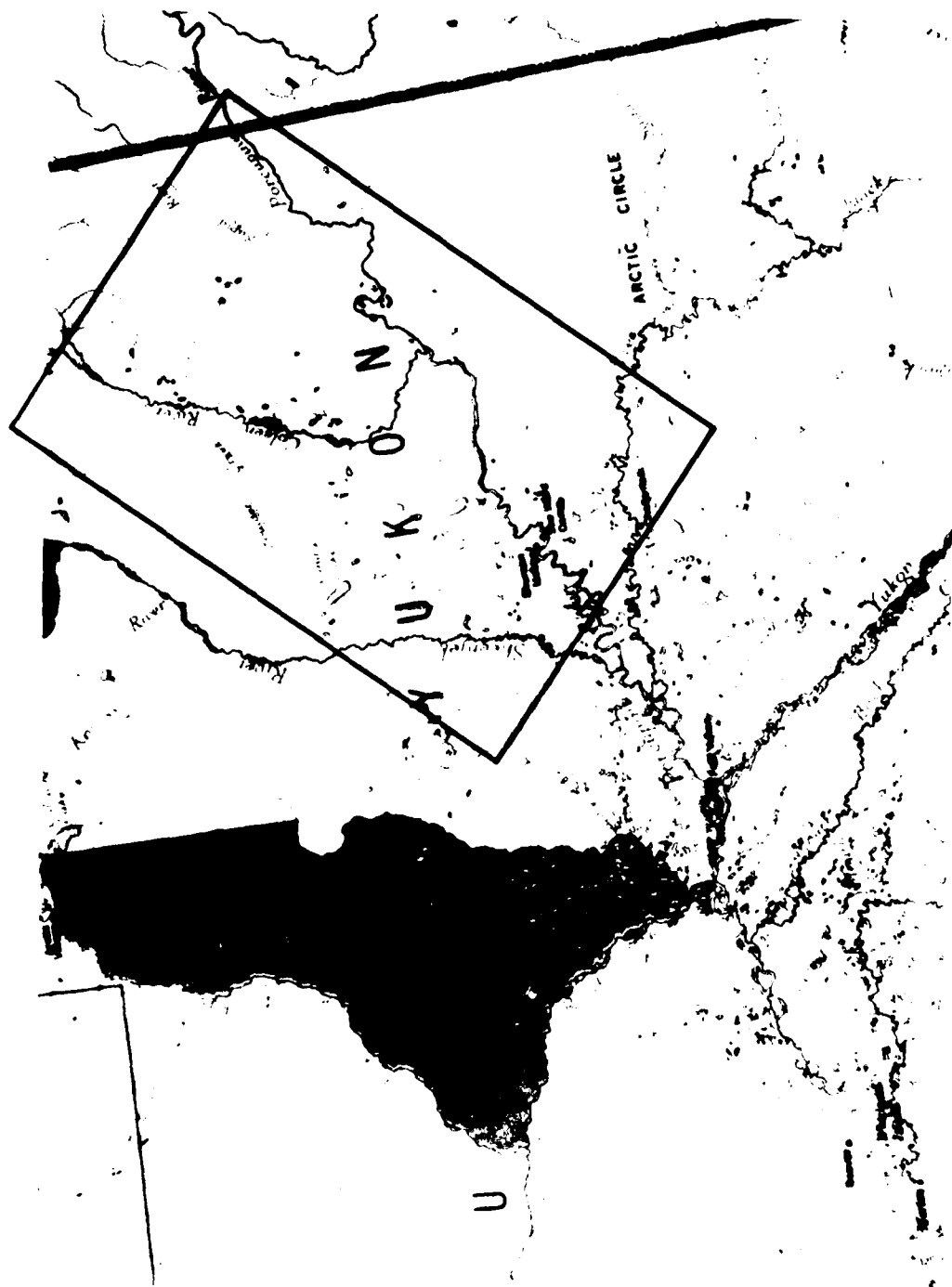


FIGURE 10 TOPOGRAPHICAL MAP OF REGION ENCOMPASSING SAR IMAGE

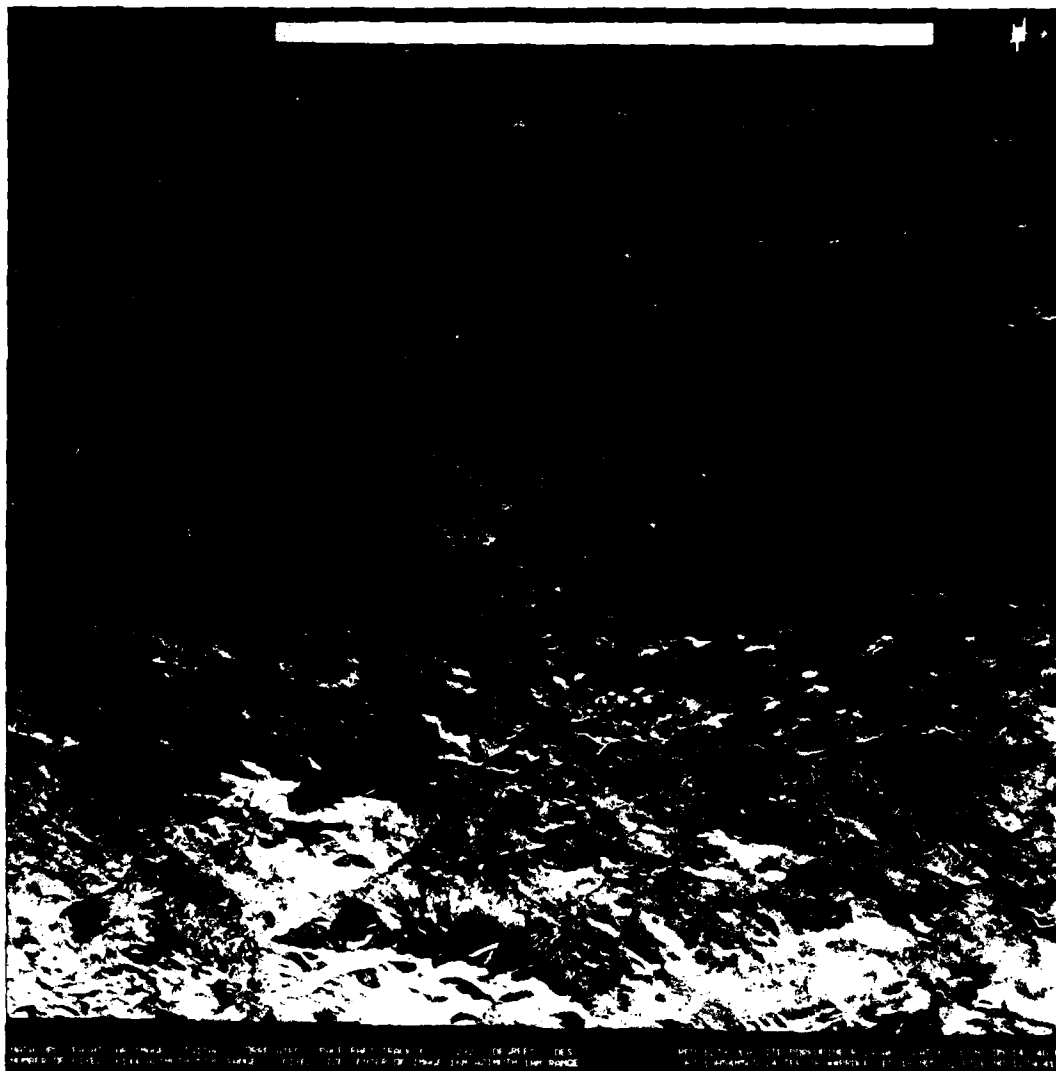


FIGURE 11 DIGITALLY PROCESSED IMAGE FOR REVOLUTION 2379

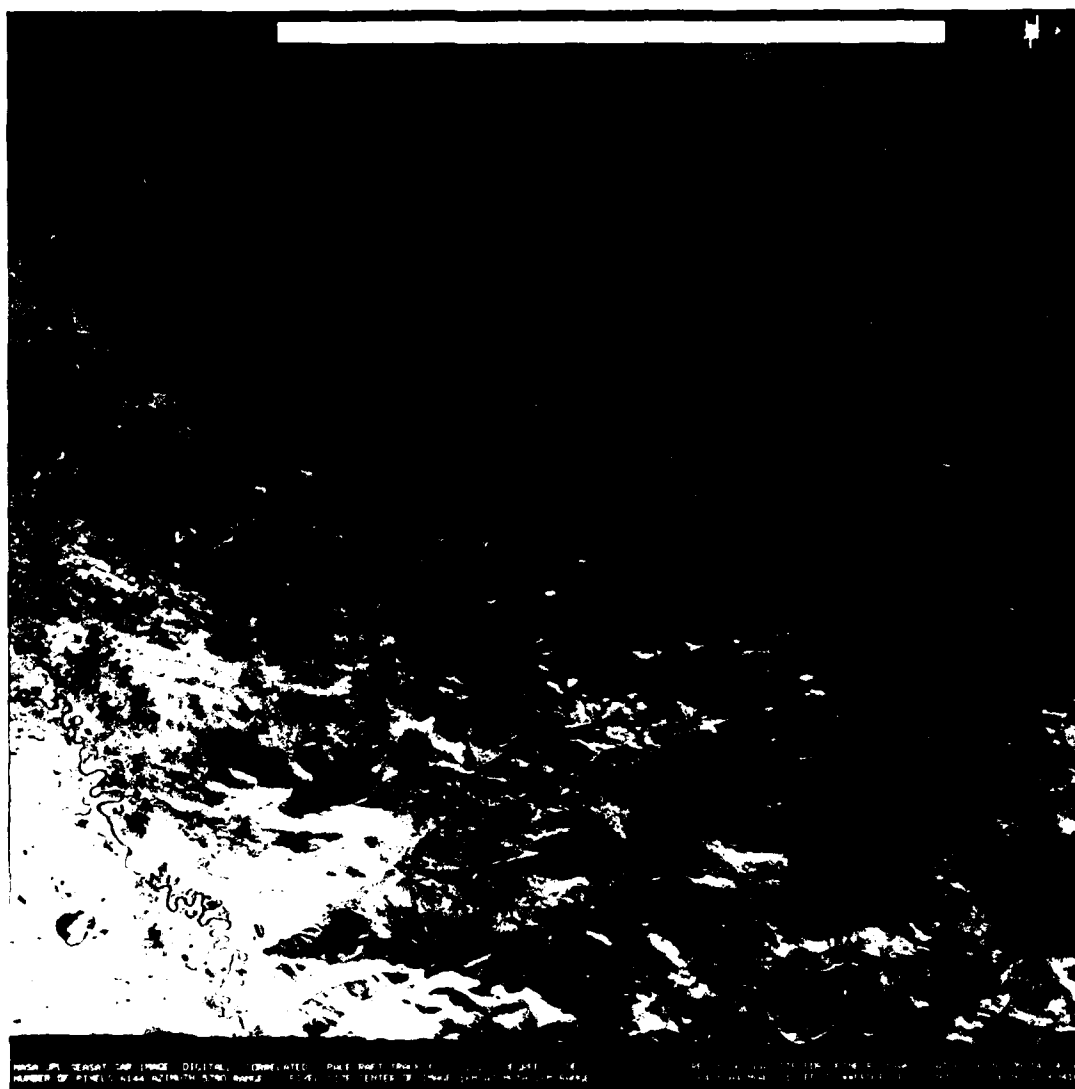


FIGURE 12 DIGITALLY PROCESSED IMAGE FOR REVOLUTION 1236

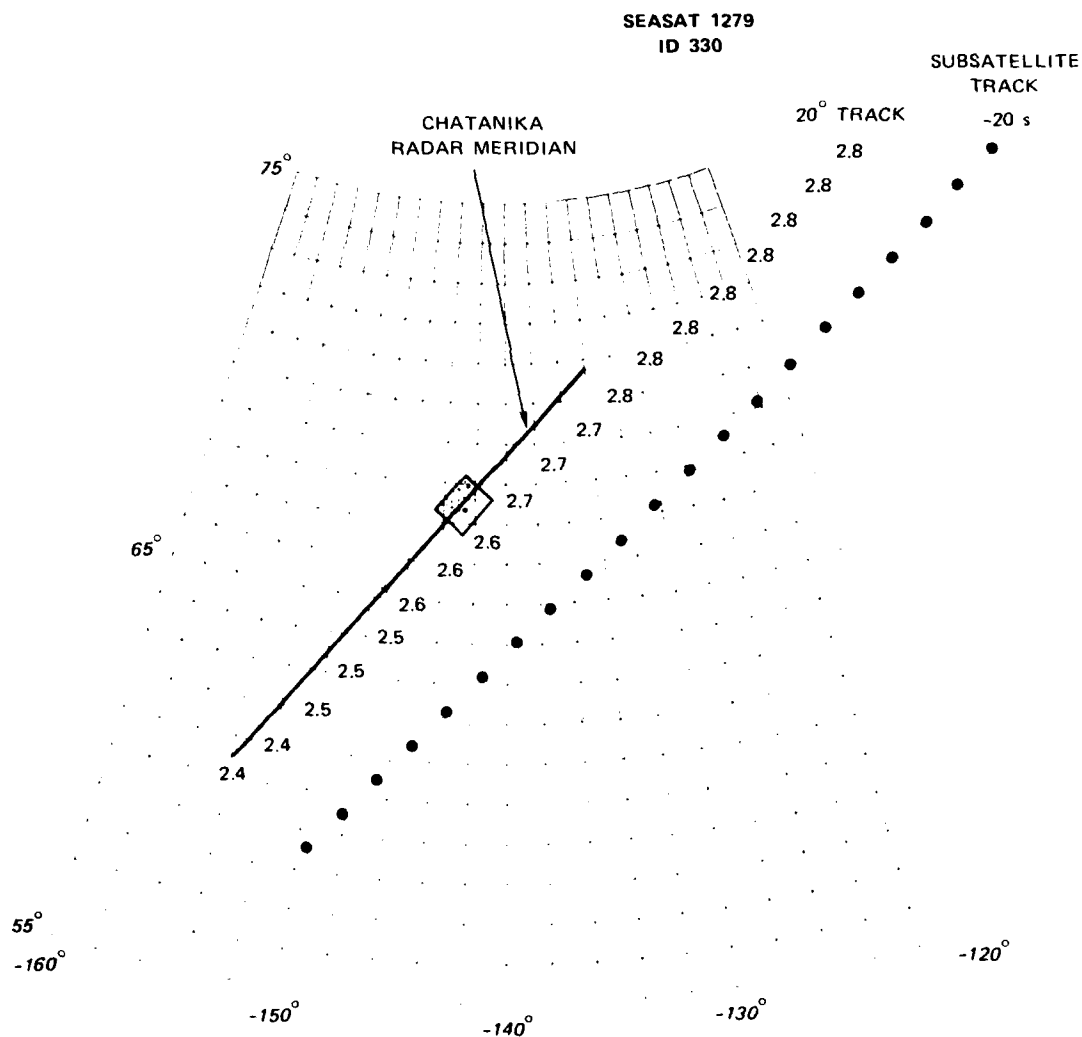


FIGURE 13 MAP GRID SHOWING LOCATIONS OF DEGRADED SAR IMAGE AND CHATANIKA MERIDIAN

The dark bar locates the meridian plane of the radar scan. The area of the SAR image is outlined, and the region of the degradation is shaded. The plane of the meridian scan intercepts the image region; however, the F-region penetration point of the structure region lies to the east of the ground image area. It is significant that the degradation was observed as an east-west protrusion into the image region.

The satellite track identifier closest to the image region occurred at 10:30. Two of the 12-minute elevation scans bracketed this period. The reconstructed meridional density contour maps are shown in Figures 14 and 15.

A highly structured enhanced F-layer is a prominent feature in both maps. From recent studies of these F-region structures, we know that they are highly unstable; moreover, although the large-scale structure maps along the L-shells, there is a considerable amount of small-scale east-west structure as predicted by Keskinen and Ossakow.¹⁷ Thus, we cannot correlate the individual blob structures with the image degradation. However, we know that scintillation-producing irregularities, of the type we have been studying intensively for several years now, were almost certainly present along the propagation path to the degraded image.

We have emphasized the data from SEASAT-A revolutions 1236 and 1279 because of the incoherent-scatter radar data that allowed us to identify the likely source region of the disturbance. Also, in our initial search of the candidate passes listed in Table 2, we were looking for image degradation of an unknown character. The tendency in the initial search was to look for loss of resolution rather than loss of contrast. The optically processed images that were used for the initial search, moreover, were processed in four strips, which often showed intensity gradients across the image.

Thus, it is reasonable to assume that a propagation-induced contrast reduction in high-latitude SAR images is present in many more of the candidate passes but was overlooked in the initial search. Indeed, Dr. Bryan Honeycutt of JPL had noted a contrast reduction in a SEASAT-A image of Banks Island during a period of high-geomagnetic activity. He attributed the effect to an auroral-activity-induced propagation disturbance.

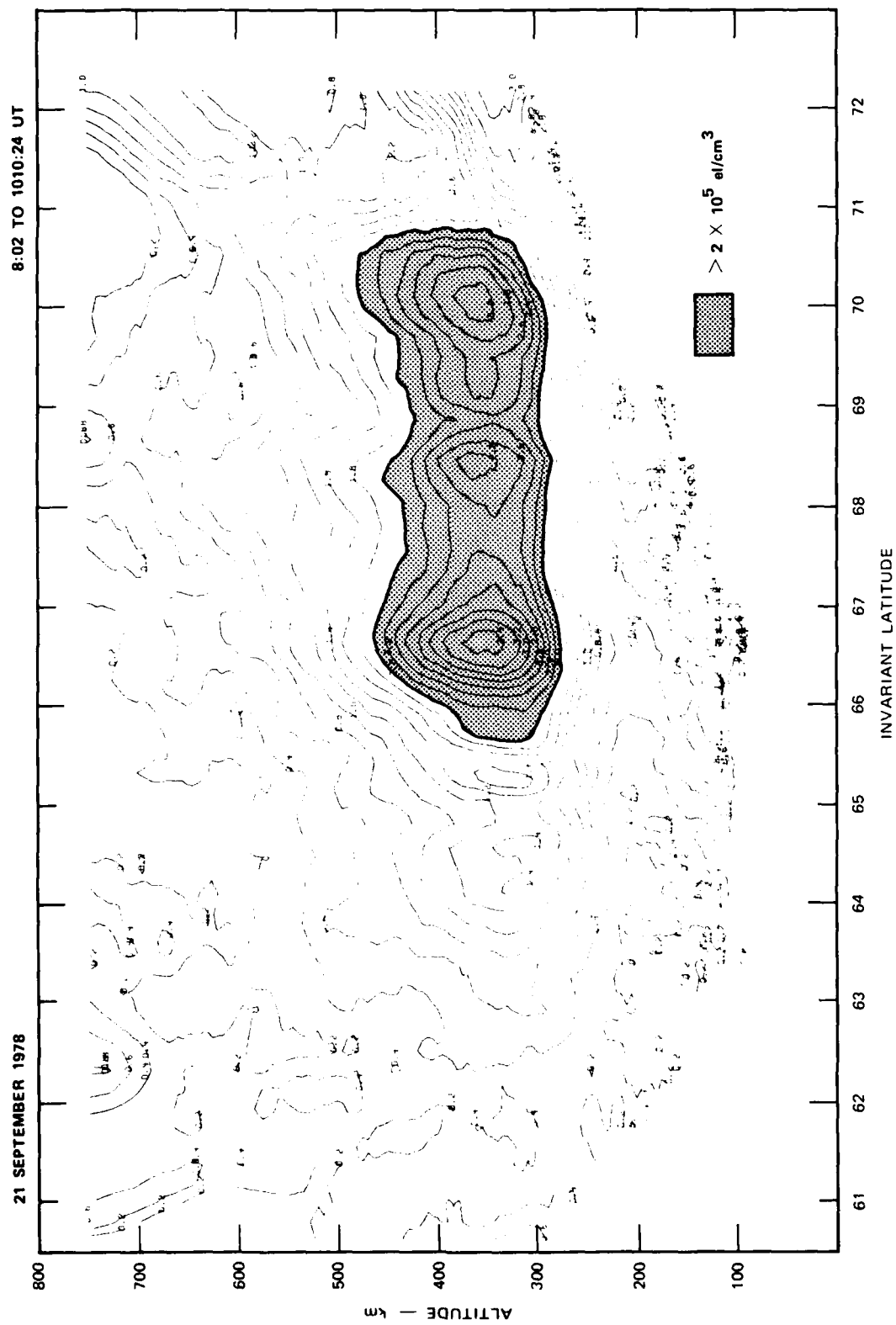


FIGURE 14 CHATANIKA RADAR MAP OF MERIDIONAL IONIZATION DISTRIBUTION PRIOR TO SAR IMAGE

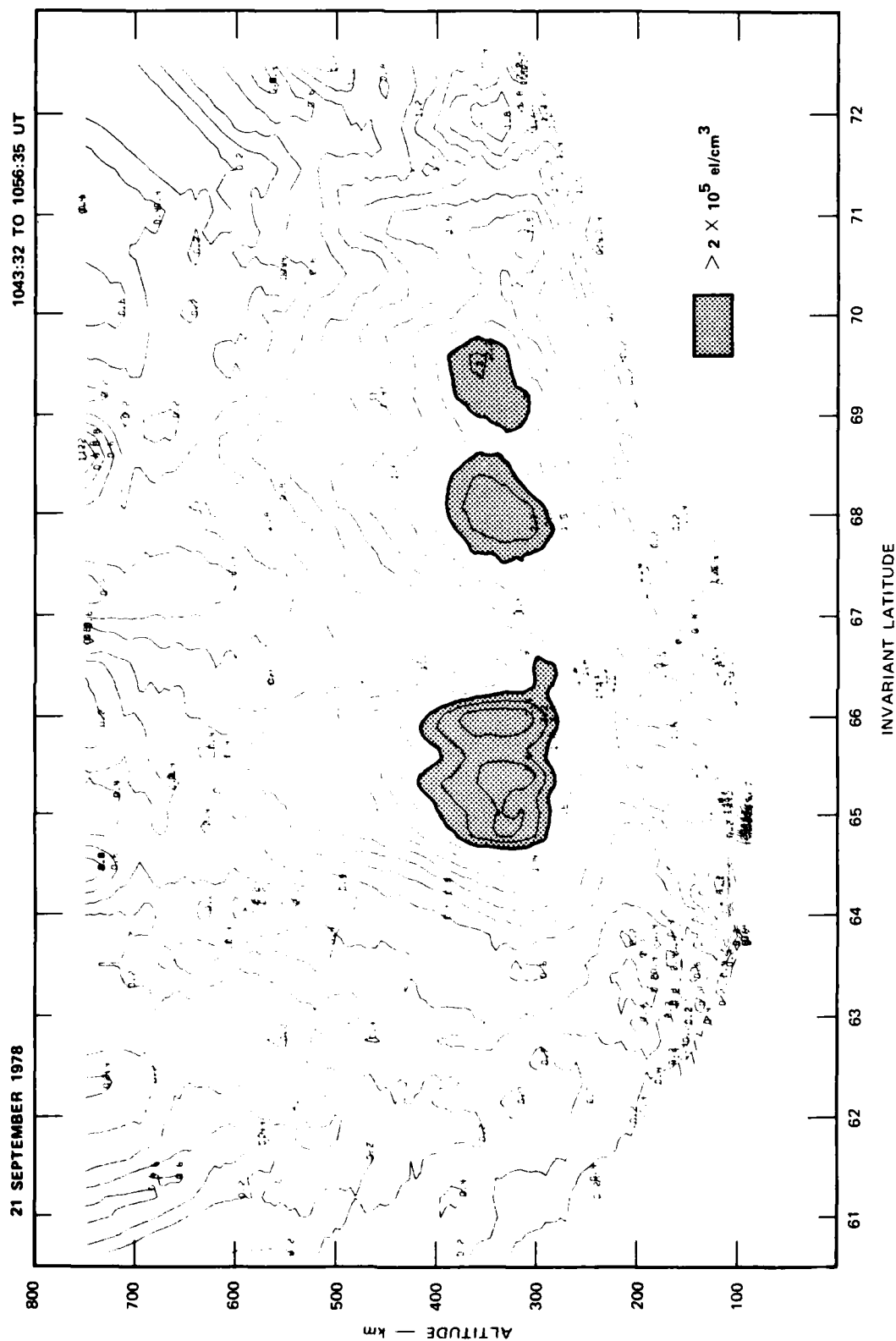


FIGURE 15 CHATANIKA RADAR MAP OF MERIDIONAL IONIZATION DISTRIBUTION AFTER SAR IMAGE

V CONCLUSIONS AND RECOMMENDATIONS

In this report we have analyzed the likely effects of propagation disturbances on satellite-borne SAR imagery. The work is an application of the general space-based radar model developed during the first phase of this contract. The principal effect of propagation disturbances is a degradation of the azimuthal component of the SAR ambiguity function. In a very severely disturbed environment, coherence bandwidth loss could also degrade the range resolution, although at L-band and higher frequencies naturally occurring disturbances will not cause such effects.

Simulations of the azimuthal degradation show that an elevated sidelobe level is the dominant effect. In an actual SAR image, the elevated sidelobes evidently reduce contrast. We showed a very good example of this effect in an image obtained from a SEASAT-A pass over Alaska with correlative incoherent-scatter radar data to identify the disturbance.

More severe disturbances, of the type commonly observed near the geomagnetic equator, would likely cause a much more severe contrast reduction, although the detailed characteristics of such disturbances should be investigated further.

A potentially important factor in the SEASAT-A image we analyzed is that the propagation disturbance occurred in a geometry for which the enhancement of the disturbance and to the known sheet-like anisotropy of the irregularities was not significant. Thus, for a more nearly meridional alignment of the satellite, the same structure could produce a more severe degradation. More elaborate simulations than those we performed in Section III should be initiated to identify the effects of the geometric dependence of propagation disturbances.

Such simulations also would provide a data source for testing more elaborate mitigation schemes. As shown in Section II, the simulations need not reproduce in complete detail the SAR data recording and processing procedures. For example, the pulse compression operation can be eliminated by assuming that the compressed pulse was actually transmitted. There is no loss of generality insofar as propagation effects are concerned.

Our preliminary analysis suggests that the degradation depends on the spatial coherence scale ℓ_0 which varies essentially linearly with frequency and that naturally occurring irregularities in the auroral zone and, particularly, near the geomagnetic equator can degrade SAR images. On the other hand, a thorough search of the SEASAT-A library of high latitude SAR data did not reveal many examples of the expected effects.

One explanation is that the disturbed regions are patchy such that the average occurrence of scintillation based on long-term morphological data exaggerates the likelihood of intense irregularities occurring at a single point. Alternatively, the focusing process used in the SAR image reconstruction may compensate for a large amount of the ionosphere-induced phase distortion.

To investigate this possibility, we propose more detailed simulations that can accommodate two-dimensional images. This will also allow us to evaluate the various measures of image degradation that are being used and determine the improvements that can be achieved by increasing frequencies and/or using image enhancement techniques.

REFERENCES

1. Rino, Charles L., Propagation effects in space-based surveillance systems, DNA Topical Report, Contract DNA001-81-C-0010, 1982.
2. Swerling, Peter, Probability of detection for fluctuating targets, RAND Corporation Research Memo RM-1217, 1954.
3. Schwartz, Mischa, Effects of signal fluctuation on the detection of pulse signals in noise, Trans. IRE, IT-2, 66, 1956.
4. Rino, C. L., J. Petriceks, R. Livingston, and C. Dawson, Data reduction and analysis of coherent satellite transmissions, Final Report, SRI International, Menlo Park, CA 94025, 1977.
5. Jordan, Rolando L., The SEASAT-A synthetic aperture radar system, IEEE Ocean. Engineer., OE-5, 154, 1980.
6. Cumming, Ian G., and John R. Bennett, Digital processing of SEASAT SAR data, IEEE Inter. Conf. on Acoust., Speech and Signal Processing, Washington, D C, 1979.
7. Yeh, Kung Chie, and Liu, Chao-Han, Radio wave scintillations in the ionosphere, Proc. IEEE, 70, 324, 1982.
8. Rino, C. L., On the application of phase screen models to the interpretation of ionospheric scintillation data, Radio Sci., 17, 855, 1982.
9. Wittwer, Major L. A., Atmospheric Effects Division, DNA, A trans-ionospheric signal specification for satellite C³ applications, In-House Report, 1980.
10. Rino, C. L., V. H. Gonzalez, and A. R. Hessing, Coherence bandwidth loss in transionospheric radio propagation, Radio Sci., 15, 245, 1981.
11. Rino, C. L., R. T. Tsunoda, J. Petriceks, R. C. Livingston, M. C. Kelley, and K. D. Baker, Simultaneous rocketborne beacon and in-situ measurements of equatorial spread F--Intermediate wavelength results, J. Geophys. Res., 86, 2411, 1981.
12. Basu, S., S. Basu, J. P. McClure, and W. B. Hanson, High-resolution topside in-situ data of electron densities and VHF/GHz scintillations in the equatorial region, J. Geophys. Res., 88, 403, 1983.

13. Rino, C. L., and J. Owen, Numerical simulations of intensity scintillation using the power law phase screen model, to be submitted to Radio Sci. in 1983.
14. Elachi, C. and D. D. Evans, Effects of random phase changes on the formation of synthetic aperture radar imagery, IEEE PGAP, 149, 1977.
15. Rino, C. L., and J. F. Vickrey, Recent results in auroral-zone scintillation studies, J. Atmos. Terr. Phys., 44, 875, 1982.
16. Livingston, R. C., C. L. Rino, J. Owen, and R. T. Tsunoda, The anisotropy of high-latitude nighttime F-region irregularities, J. Geophys. Res., 87, 10, 519, 1983.
17. Keskinen, M. I., and S. L. Ossakow, Theories of high-latitude ionospheric irregularities: A review, submitted to Radio Sci., 1982.

DISTRIBUTION LIST

DEPARTMENT OF DEFENSE

Assistant to the Secretary of Defense
Atomic Energy
ATTN: Executive Asst

Command & Control Technical Ctr
ATTN: C-312, R. Mason
ATTN: C-650, G. Jones
ATTN: C-650
3 cy ATTN: C-650, W. Heidig

Defense Communications Agency
ATTN: Code 230
ATTN: Code 205
ATTN: J300 for Yen-Sun Fu

Defense Communications Engr Ctr
ATTN: Code R410, R. Craighill
ATTN: Code R410, N. Jones
ATTN: Code R410
ATTN: Code R123

Defense Intelligence Agency
ATTN: Dir
ATTN: DB-4C, E. O'Farrell
ATTN: DB, A. Wise
ATTN: DT-1B
ATTN: DC-7B

Defense Nuclear Agency
ATTN: NAFD
ATTN: RAAE, P. Lunn
ATTN: STNA
ATTN: RAE
ATTN: NATD
3 cy ATTN: RAAE
4 cy ATTN: TITL

Defense Tech Info Ctr
12 cy ATTN: DD

Deputy Under Secretary of Defense
Comm, Cmd, Cont & Intell
ATTN: Dir of Intell Sys

Field Command
Defense Nuclear Agency, Det 1
Lawrence Livermore Lab
ATTN: FC-1

Field Command
Defense Nuclear Agency
ATTN: FCTT, W. Summa
ATTN: FCTXL
ATTN: FCTT, G. Ganong
ATTN: FCPR

Interservice Nuclear Weapons School
ATTN: ITV

Joint Chiefs of Staff
ATTN: C35
ATTN: C35, Evaluation Office, HD00

DEPARTMENT OF DEFENSE (Continued)

Joint Strat Tgt Planning Staff
ATTN: JLA, Threat Applications Div
ATTN: JLTW-2

WWMCCS System Engineering Org
ATTN: J. Hoff

Under Secretary of Defense for Rsch & Engrg
ATTN: Strategic & Space Sys, (OS)
ATTN: Strat & Theater Nuc Forces, B. Stephan

National Security Agency
ATTN: W-32, O. Bartlett
ATTN: B-3, F. Leonard

DEPARTMENT OF THE ARMY

Assistant Chief of Staff for Automation & Comm
ATTN: DAMO-C4, P. Kenny

Atmospheric Sciences Lab
ATTN: DELAS-EO, F. Niles

BMD Advanced Technolgy Ctr
ATTN: ATC-R, D. Russ
ATTN: ATC-T, M. Capps
ATTN: ATC-O, W. Davies
ATTN: ATC-R, W. Dickinson

BMD Systems Command
ATTN: BMDSC-HLE, R. Webb
2 cy ATTN: BMDSC-HW

Deputy Chief of Staff for Ops & Plans
ATTN: DAMO-RQC, C2 Div

Harry Diamond Labs
ATTN: Chief Div 20000
ATTN: DELHD-NW-R, R. Williams, 22000

US Army Chemical School
ATTN: ATZN-CM-CS

US Army Comm-Elec Engrg Instal Agency
ATTN: CCC-CED-CCO, W. Neuendorf
ATTN: CCC-EMEC-PED, G. Lane

US Army Communications Cmd
ATTN: CC-OPS-WR, H. Wilson
ATTN: CC-OPS-W

US Army Comm R&D Cmd
ATTN: DRDCO-COM-RY, W. Kesselman

US Army Foreign Science & Tech Ctr
ATTN: DRXST-SD

US Army Materiel Dev & Readiness Cmd
ATTN: DRCLDC, J. Bender

US Army Nuc & Chem Agency
ATTN: Library

DEPARTMENT OF THE ARMY (Continued)

US Army Satellite Comm Agency
ATTN: Doc Con

US Army TRADOC Sys Analysis Actvy
ATTN: ATAA-PL
ATTN: ATAA-TDC
ATTN: ATAA-TCG, F. Payan, Jr

US Army White Sands Missile Range
ATTN: STEWS-TN-N, K. Cummings

USA Missile Cmd
ATTN: DRSM1-YSO, J. Gamble

DEPARTMENT OF THE NAVY

Joint Cruise Missiles Project Ofc
ATTN: JCMG-707

Naval Air Systems Cmd
ATTN: PMA 271

Naval Electronic Systems Cmd
ATTN: PME 106-4, S. Kearney
ATTN: PME 117-20
ATTN: Code 3101, T. Hughes
ATTN: PME 106-13, T. Griffin
ATTN: PME 117-2013, G. Burnhart
ATTN: Code 501A
ATTN: 117-211, B. Kruger

Naval Intelligence Support Ctr
ATTN: NISC-50

Naval Ocean Systems Ctr
ATTN: Code 532
ATTN: Code 5323, J. Ferguson
ATTN: Code 5322, M. Paulson

Naval Rsch Lab
ATTN: Code 4790
ATTN: Code 4730, S. Ossakow
ATTN: Code 4137
ATTN: Code 7500, S. Wald
ATTN: Code 4700
ATTN: Code 4720, J. Davis
ATTN: Code 7950, J. Goodman
ATTN: Code 6700

Naval Space Surveillance Sys
ATTN: J. Burton

Naval Surface Weapons Ctr
ATTN: Code F31

Naval Telecommunications Cmd
ATTN: Code 341

Office of the Deputy Chief of Naval Ops
ATTN: NOP 931N
ATTN: NOP 654 Strat Eval & Anal Br
ATTN: NOP 141D

Office of Naval Rsch
ATTN: Code 414, G. Joiner
ATTN: Code 412, W. Condell

DEPARTMENT OF THE NAVY (Continued)

Strategic Systems Project Office
ATTN: NSP-2141
ATTN: NSP-43
ATTN: NSP-2722

Theater Nuclear Warfare Prj Office
ATTN: PM-23, D. Smith

DEPARTMENT OF THE AIR FORCE

Air Force Geophysics Lab
ATTN: OPR, H. Gardiner
ATTN: OPR-1
ATTN: LKB, K. Champion
ATTN: CA, A. Stair
ATTN: PHY, J. Buchau
ATTN: R. Babcock
ATTN: R. O'Neil

Air Force Tech Applications Ctr
ATTN: TN

Air Force Weapons Lab
ATTN: SUL
ATTN: NTYC
ATTN: NTN

Air Force Wright Aeronautical Lab/AAAD
ATTN: W. Hunt
ATTN: A. Johnson

Air Logistics Cmd
ATTN: CO-ALC/MM

Air University Library
ATTN: AUL-LSE

Assistant Chief of Staff
Studies & Analyses
ATTN: AF/SASC, W. Kraus
ATTN: AF/SASC, C. Rightmeyer

Ballistic Missile Office
ATTN: ENSN
ATTN: SYC, D. Lwan
ATTN: ENSN, W. Wilson

Deputy Chief of Staff
Rsch, Dev & Acq
ATTN: AFRDP
ATTN: AFRDS, Space Sys & C3 Dir
ATTN: AFRDS, Space Sys & C3 Dir

Deputy Chief of Staff
Plans & Operations
ATTN: AFXOICD
ATTN: AFXOKS
ATTN: AFXORT

Headquarters
Electronic Systems Div
ATTN: ESD/SCTE, J. Clark
ATTN: OCT-4, J. Deas
ATTN: SCS-1, C. Vinkels
ATTN: SCS-1E

DEPARTMENT OF THE AIR FORCE (Continued)

Foreign Technology Div
ATTN: TQTD, B. Ballard
ATTN: NIIS, Library

Rome Air Dev Ctr
ATTN: OCS, V. Coyne
ATTN: TSLD

Rome Air Dev Ctr
ATTN: EEP, J. Rasmussen

Headquarters
Space Command
ATTN: DC, T. Long

Space Div
ATTN: YGJB, W. Mercer
ATTN: YKM, E. Norton
ATTN: YKM, W. Alexander

Strategic Air Command
ATTN: NRT
ATTN: DCXT, T. Jorgensen
ATTN: XPFS
ATTN: DCX
ATTN: ADWAT, R. Wittler
ATTN: XPFS

DEPARTMENT OF ENERGY

Department of Energy
ATTN: DP-10

OTHER GOVERNMENT AGENCIES

Central Intelligence Agency
ATTN: OSWR/NED
ATTN: OSWR/SSD for A. Feuerpfel

Department of Commerce
National Bureau of Standards
ATTN: Sec Ofc for R. Moore

Department of Commerce
National Oceanic & Atmospheric Admin
ATTN: R. Grubb

National Telecommunications & Info Admin
ATTN: L. Berry
ATTN: A. Jean
ATTN: W. Utlaut

Department of State
Office of International Security Policy
ATTN: PM/STM

NATO

NATO School, SHAPE
ATTN: US Documents Officer

DEPARTMENT OF ENERGY CONTRACTORS

EG&G, Inc
Attention Doc Con for
ATTN: J. Colvin
ATTN: D. Wright

DEPARTMENT OF ENERGY CONTRACTORS (Continued)

University of California
Lawrence Livermore National Lab
ATTN: L-389, R. Ott
ATTN: L-31, R. Hager
ATTN: Tech Info Dept, Library

Los Alamos National Lab
ATTN: MS 670, J. Hopkins
ATTN: P. Keaton
ATTN: MS 664, J. Zinn
ATTN: T. Kunkle, ESS-5
ATTN: R. Jeffries
ATTN: D. Simons
ATTN: J. Wolcott

Sandia National Labs
ATTN: B. Murphey
ATTN: T. Cook

Sandia National Labs
ATTN: D. Thornbrough
ATTN: Tech Library, 3141
ATTN: D. Dahlgren
ATTN: Space Project Div
ATTN: Org 4231, T. Wright
ATTN: Org 1250, W. Brown

DEPARTMENT OF DEFENSE CONTRACTORS

Aerospace Corp
ATTN: V. Josephson
ATTN: R. Slaughter
ATTN: T. Salmi
ATTN: I. Garfunkel
ATTN: Y. Cho
ATTN: J. Strauss
ATTN: D. Olsen

Analytical Systems Engrg Corp
ATTN: Radio Sciences

Analytical Systems Engrg Corp
ATTN: Security

BDM Corp
ATTN: T. Neighbors
ATTN: L. Jacobs

Berkeley Rsch Associates, Inc
ATTN: C. Prettie
ATTN: J. Workman
ATTN: S. Brecht

Boeing Aerospace Co
ATTN: MS/87-63, D. Clauson

Boeing Co
ATTN: G. Hall
ATTN: S. Tashird

BR Communications
ATTN: J. McLaughlin

University of California at San Diego
ATTN: H. Booker

DEPARTMENT OF DEFENSE CONTRACTORS (Continued)

Charles Stark Draper Lab, Inc
ATTN: J. Gilmore
ATTN: D. Cox
ATTN: A. Tetewski

Computer Sciences Corp
ATTN: F. Eisenbarth

Comsat Labs
ATTN: G. Hyde
ATTN: D. Fang

Cornell University
ATTN: D. Farley, Jr
ATTN: M. Kelly

E-Systems, Inc
ATTN: R. Berezdivin

Electrospace Systems, Inc
ATTN: H. Logston
ATTN: P. Phillips

EOS Technologies, Inc
ATTN: B. Gabbard

General Electric Co
ATTN: A. Steinmayer
ATTN: C. Zierdt

General Electric Co
ATTN: G. Millman

General Rsch Corp
ATTN: B. Bennett

Geo Ctrs, Inc
ATTN: E. Marnam

GTE Communications Products Corp
ATTN: R. Steinhoff

GTE Communications Products Corp
ATTN: J. Concordia
ATTN: L. Fohlberg

Harris Corp
ATTN: E. Knick

Honeywell, Inc
ATTN: G. Terry, Avionics Dept
ATTN: A. Kearns, MS924-3

Horizons Technology, Inc
ATTN: R. Kruger

HSS, Inc
ATTN: D. Hansen

IBM Corp
ATTN: H. Ulander

Institute for Defense Analyses
ATTN: J. Acin
ATTN: F. Bauer
ATTN: H. Wolfhard
ATTN: H. Gates

DEPARTMENT OF DEFENSE CONTRACTORS (Continued)

International Tel & Telegraph Corp
ATTN: Tech Library

International Tel & Telegraph Corp
ATTN: G. Wetmore

JAYCOR
ATTN: J. Sperling

Johns Hopkins University
ATTN: T. Evans
ATTN: K. Potocki
ATTN: J. Newland
ATTN: P. Komiske
ATTN: J. Phillips

Kaman Tempo
ATTN: B. Cambill
ATTN: E. Schwartz
ATTN: DASIAC
ATTN: J. Devore
ATTN: W. McNamara

Kaman Tempo
ATTN: DASIAC

Litton Systems, Inc
ATTN: B. Zimmer

Lockheed Missiles & Space Co, Inc
ATTN: J. Eumer
ATTN: R. Sears

Lockheed Missiles & Space Co, Inc
ATTN: Dept 60-12
/ by ATTN: D. Churchill, Dept 62-A1

M.I.T. Lincoln Lab
ATTN: D. Towle

MA/COM Linkabit Inc
ATTN: A. Vitberbi
ATTN: H. Van Trees
ATTN: I. Jacobs

Magnavox Govt & Indus Electronics Co
ATTN: G. White

McDonnell Douglas Corp
ATTN: Tech Library Svcs
ATTN: W. Olson
ATTN: R. Halprin

Meteor Communications Corp
ATTN: R. Leader

Mission Rsch Corp
ATTN: C. Lauer
ATTN: Tech Library
ATTN: F. Fajen
ATTN: R. Kilb
ATTN: S. Gutsche
ATTN: R. Bigoni
ATTN: R. Bogusch
ATTN: F. Guigliano
ATTN: G. McCartor
ATTN: D. Fnepp
ATTN: R. Hendrick

DEPARTMENT OF DEFENSE CONTRACTORS (Continued)

Mitre Corp
ATTN: MS J104, M. Dresp
ATTN: A. Kymmel
ATTN: G. Harding
ATTN: C. Callahan

Mitre Corp
ATTN: W. Hall
ATTN: J. Wheeler
ATTN: M. Horrocks
ATTN: W. Foster

Pacific-Sierra Rsch Corp
ATTN: E. Field, Jr
ATTN: F. Thomas
ATTN: H. Brode, Chairman SAGE

Pennsylvania State University
ATTN: Ionospheric Rsch Lab

Photometrics, Inc
ATTN: I. Kofsky

Physical Dynamics, Inc
ATTN: E. Fremouw

Physical Rsch, Inc
ATTN: R. Deliberis
ATTN: T. Stephens

R&D Associates
ATTN: R. Turco
ATTN: W. Karzas
ATTN: H. Ory
ATTN: C. Greifinger
ATTN: M. Gantsweg
ATTN: F. Gilmore
ATTN: W. Wright
ATTN: P. Haas

R&D Associates
ATTN: B. Yoon

Rand Corp
ATTN: E. Bedrozian
ATTN: C. Crain
ATTN: P. Davis

Rand Corp
ATTN: B. Bennett

Riverside Rsch Institute
ATTN: V. Trapani

Rockwell International Corp
ATTN: R. Buckner

Rockwell International Corp
ATTN: S. Quilici

DEPARTMENT OF DEFENSE CONTRACTORS (Continued)

Science Applications, Inc
ATTN: M. Cross

Science Applications, Inc
ATTN: J. Cockayne

SRI International
ATTN: R. Tsunoda
ATTN: J. Vickrey
ATTN: W. Chesnut
ATTN: R. Leadabrand
ATTN: R. Livingston
ATTN: D. McDaniels
ATTN: M. Baron
ATTN: G. Price
ATTN: D. Neilson
ATTN: A. Burns
ATTN: W. Jaye
ATTN: J. Petrickes
ATTN: G. Smith
4 cy ATTN: C. Rino
4 cy ATTN: V. Gonzales

Stewart Radiance Lab
ATTN: J. Ulwick

Technology International Corp
ATTN: W. Boquist

Toyon Rsch Corp
ATTN: J. Ise
ATTN: J. Garbarino

Tri-Com, Inc
ATTN: D. Murray

TRW Electronics & Defense Sector
ATTN: R. Plebuch
ATTN: G. Kirchner

Utah State University
Attention Sec Control Ofc for
ATTN: K. Baker, Dir Atmos & Space Sci
ATTN: L. Jensen, Elec Eng Dept
ATTN: D. Burt
ATTN: A. Steed

VisiDyne, Inc
ATTN: C. Humphrey
ATTN: C. Shepard
ATTN: W. Reidy
ATTN: J. Carpenter

Science Applications, Inc
ATTN: L. Linson
ATTN: D. Hamlin
ATTN: C. Smith
ATTN: E. Straker